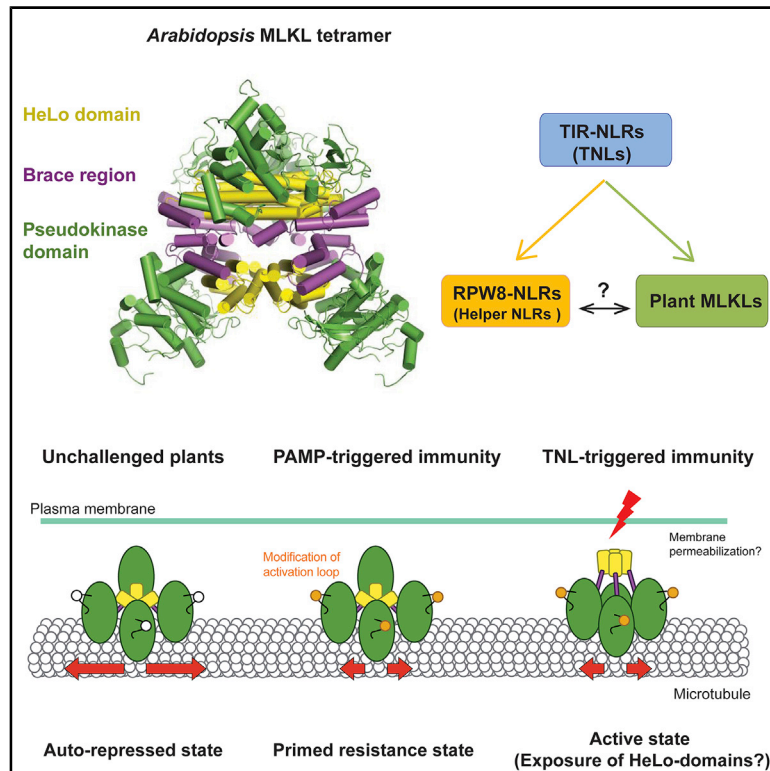# Cell Host & Microbe

Discovery of a Family of Mixed Lineage Kinase Domain-like Proteins in Plants and Their Role in Innate Immune Signaling

Graphical Abstract

Authors

Lisa K. Mahdi, Menghang Huang, Xiaoxiao Zhang, ..., Paul Schulze-Lefert, Jijie Chai, Takaki Maekawa

Correspondence

maekawa@mpipz.mpg.de

In Brief

Mahdi et al. discover a protein family resembling the vertebrate necroptosis mediator MLKL in plants. *Arabidopsis* MLKLs (*At*MLKLs) promote pathogen resistance mediated by TIR-type NLRs. Structural analysis suggests an auto-repressed tetrameric state and although *At*MLKL's HeLo domain can elicit cell death, this function is dispensable for immunity.

Highlights

- Plant genomes encode a family of proteins resembling animal necroptosis mediator MLKL

- *Arabidopsis* MLKLs (*At*MLKLs) promote pathogen resistance mediated by TIR-type NLRs

- Cryo-EM structure of *At*MLKL reveals tetramers, which represents an auto-repressed state

- *At*MLKLs HeLo domain can elicit cell death but this is dispensable for immune function

CellPress

Discovery of a Family of Mixed Lineage Kinase Domain-like Proteins in Plants and Their Role in Innate Immune Signaling

Lisa K. Mahdi,[1,10,11] Menghang Huang,[2,10] Xiaoxiao Zhang,[2,10] Ryohei Thomas Nakano,[1,3] Leïla Brulé Kopp,[1,4] Isabel M.L. Saur,[1] Florence Jacob,[1,5,12] Viera Kovacova,[6,13] Dmitry Lapin,[1] Jane E. Parker,[1,3] James M. Murphy,[7,8] Kay Hofmann,[9] Paul Schulze-Lefert,[1,3] Jijie Chai,[1,2,3] and Takaki Maekawa[1,11,14,*]

[1]Max Planck Institute for Plant Breeding Research, 50829 Cologne, Germany
[2]Beijing Advanced Innovation Center for Structural Biology, Tsinghua-Peking Joint Center for Life Sciences, Center for Plant Biology, School of Life Sciences, Tsinghua University, 100084 Beijing, China
[3]Cluster of Excellence on Plant Sciences (CEPLAS), Max Planck Institute for Plant Breeding Research, 50829 Cologne, Germany
[4]École normale supérieure Paris, 75230 Paris Cedex 05, France
[5]Institute of Plant Sciences Paris-Saclay, Centre National de la Recherche Scientifique, Institut National de la Recherche Agronomique, Université Paris Sud, Université d'Evry, Université Paris Diderot, Sorbonne Paris-Cité, Université Paris-Saclay, 91405 Orsay, France
[6]University of Cologne, Cologne Excellence Cluster on Cellular Stress Responses in Aging-Associated Diseases (CECAD), University of Cologne, 50931 Cologne, Germany
[7]Walter and Eliza Hall Institute of Medical Research, 1G Royal Parade, Parkville, VIC 3052, Australia
[8]Department of Medical Biology, University of Melbourne, Parkville, VIC 3052, Australia
[9]Institute for Genetics, University of Cologne, 50674 Cologne, Germany
[10]These authors contributed equally
[11]Present address: Institute for Plant Sciences, University of Cologne, Cologne 50674, Germany
[12]Present address: PalmElit Sas, F-34980 Montferrier-sur-Lez, France
[13]Present address: Institute for Biological Physics, University of Cologne, Cologne 50937, Germany
[14]Lead Contact
*Correspondence: maekawa@mpipz.mpg.de
https://doi.org/10.1016/j.chom.2020.08.012

SUMMARY

HeLo domain-containing mixed lineage kinase domain-like protein (MLKL), a pseudokinase, mediates necroptotic cell death in animals. Here, we report the discovery of a conserved protein family across seed plants that structurally resembles vertebrate MLKL. The *Arabidopsis* genome encodes three MLKLs (*At*MLKLs) with overlapping functions in disease resistance mediated by Toll-interleukin 1-receptor domain intracellular immune receptors (TNLs). The HeLo domain of *At*MLKLs confers cell death activity but is dispensable for immunity. Cryo-EM structures reveal a tetrameric configuration, in which the HeLo domain is buried, suggestive of an auto-repressed complex. The mobility of *At*MLKL1 along microtubules is reduced by chitin, a fungal immunity-triggering molecule. An *At*MLKL1 phosphomimetic variant exhibiting reduced mobility enhances immunity. Coupled with the predicted presence of HeLo domains in plant helper NLRs, our data reveal the importance of HeLo domain proteins for TNL-dependent immunity and argue for a cell death-independent immune mechanism mediated by MLKLs.

INTRODUCTION

Decades of research have revealed notable similarities between the innate immune systems of the plant and animal kingdoms, including cell surface (Nürnberger and Brunner, 2002) and intracellular receptors (Jones et al., 2016; Maekawa et al., 2011b). Many cell surface receptors recognize pathogen-associated molecular patterns (PAMPs), epitopes that are often well conserved across members of a given microbial group (e.g., chitin from fungal cell walls) (Boutrot and Zipfel, 2017). Intracellular receptors are exemplified by nucleotide-binding leucine-rich repeat receptors (NLRs), which primarily detect pathogen

race-specific effectors in plants and PAMPs in animals (Maekawa et al., 2011b). Despite functional similarities, PAMP receptors and NLRs are thought to have evolved independently in plants and animals (Urbach and Ausubel, 2017; Zipfel, 2008).

Regulated cell death is intimately connected with innate immunity in plants and animals (Chan et al., 2015; Coll et al., 2011; van Doorn, 2011). A shared feature of several proteins involved in regulated cell death in plants, animals, and fungi is a four-helix bundle structure called the HeLo domain (Daskalov et al., 2016). HeLo domain-containing MLKL (mixed lineage kinase domain-like protein) mediates necroptosis in animals (Sun et al., 2012; Zhao et al., 2012; Murphy et al., 2013), a form

of regulated cell death that is proposed to combat pathogens by promoting the release of pro-inflammatory molecules (Petrie et al., 2019; Vanden Berghe et al., 2014). Necroptosis is initiated by plasma membrane-resident death receptors, with downstream activation of receptor-interacting serine/threonine-protein kinases (RIPKs) leading to the phosphorylation of the pseudokinase domain of the terminal pathway effector, MLKL (Petrie et al., 2019; Vanden Berghe et al., 2014). This process results in the assembly of monomeric MLKL into pro-necroptotic oligomers (Petrie et al., 2017, 2018) that translocate to the plasma membrane where oligomerized HeLo domains interfere with membrane integrity (Chen et al., 2014; Dondelinger et al., 2014; Hildebrand et al., 2014; Quarato et al., 2016; Wang et al., 2014). The extent to which regulated cell death in plants and animals is directly responsible for disease resistance is under debate (Bendahmane et al., 1999; Chan et al., 2015; Coll et al., 2010; Pearson and Murphy, 2017).

Three major classes of plant NLRs, TNL, CNL, and RNL, respectively, are defined by the presence of either a Toll-interleukin 1 receptor (TIR)-like domain, a coiled-coil (CC) domain or a RPW8-like CC domain at the N-terminus (Jacob et al., 2013; Jubic et al., 2019; Maekawa et al., 2011b). Due to a predicted structural resemblance, it has been postulated that RPW8-like domains within RNLs are functionally similar to the HeLo domains of MLKLs (Barragan et al., 2019; Bentham et al., 2018; Daskalov et al., 2016; Jubic et al., 2019; Li et al., 2020). While TNL-triggered immunity can recruit RNLs of the ADR1 (activated disease resistance 1) and NRG1 (N-required gene 1) families and EDS1 (enhanced disease susceptibility 1) for downstream signaling (Castel et al., 2019; Collier et al., 2011; Falk et al., 1999; Lapin et al., 2019; Qi et al., 2018; Wu et al., 2019), CNL-triggered immunity can be uncoupled from these factors (Aarts et al., 1998; Bonardi et al., 2011). Therefore, the genetic requirements for TNL- and CNL-triggered immunity are largely different.

In this study, we report a family of HeLo domain-containing proteins that are fused to a pseudokinase domain. We have named the members of this protein family plant MLKLs, as their modular structure resembles that of vertebrate MLKL. Unlike necroptosis mediated by vertebrate MLKLs, plant MLKL-mediated immunity can be separated from host cell death. Furthermore, our data point to a cooperative action of two plant HeLo domain protein families, namely plant MLKLs and RNLs, in TNL-triggered immunity.

RESULTS

MLKL Proteins in the Plant Kingdom

To identify novel immune regulators in plants, we searched for HeLo-domain-containing proteins in plant genomes by comparing Hidden Markov models. This analysis identified a protein family that is highly conserved across seed plants (Figure 1; Table S1; Data S1), with a modular structure resembling MLKL (Figure 1A). The kinase-like domain lacks canonical residues known to underlie phosphoryl transfer (Manning et al., 2002) (Figure 1B), suggestive of a catalytically inactive pseudokinase (Petrie et al., 2019). Hereafter, we refer to these proteins as plant MLKLs. Plant MLKLs additionally possess an extended serine-rich region of varying length without similarity to known

domains after the pseudokinase domain (Figure 1A; Data S1). Plant MLKLs separate into two subfamilies based on sequence similarity (Figure 1D). Unlike animals, which possess only one *MLKL* gene (https://www.ensembl.org), *Arabidopsis thaliana* harbors three *MLKL* genes with *AtMLKL1* and *AtMLKL2* in subfamily I and *AtMLKL3* belonging to subfamily II (Figures 1C and 1D).

Oligomerization of Plant MLKL Proteins *In Vitro*

To explore similarities between plant and animal MLKLs, we expressed *At*MLKL2 and *At*MLKL3 for structural analysis using cryo-electron microscopy (cryo-EM) (Figures 2 and S1). In gel filtration, both proteins eluted at an estimated molecular weight corresponding to tetramers (Figures 2A and S1A). This contrasts with the vertebrate MLKL protein, which displayed heterogeneity in a similar assay (Wang et al., 2014; Petrie et al., 2018). Representative 2D projection views indicate that both *At*MLKL oligomers form a triangle-like architecture with a 2-fold symmetry (Figures S1B, S1C, S1F, and S1G). Further 3D classification and refinement generated electrostatic potential density of oligomeric *At*MLKL2 and *At*MLKL3 with a global resolution of 4.1 Å (Figure S1E) and 3.4 Å (Figures 2B and S1I), respectively, based on the gold Fourier Shell correlation standard (Figures S1D and S1H). The 3D reconstructions show that both *At*MLKL2 and *At*MLKL3 oligomers are composed of four MLKL molecules (Figures 2C and S2A), confirming that these form tetramers. Tetramerization of *At*MLKL2 or *At*MLKL3 results in formation of a pyramid-like structure. Structural alignment of the two final models indicates that the tetramers formed by the two subfamily members are nearly identical (Figures S2A and S2B). As the quality of the density of *At*MLKL3 is superior for model building, we limited our structural analysis to *At*MLKL3.

Structural Analysis of Plant *At*MLKL3

*At*MLKL3 protomers possess the same domain architecture as mammalian MLKL with an N-terminal HeLo domain (or four-helix bundle), a C-terminal pseudokinase domain, and a helix-containing "brace" region that connects these domains. The N-terminal HeLo domain of *At*MLKL3 superimposed well with the HeLo domains of mouse and human MLKL (mMLKL and hMLKL, respectively; Figure 3A). This observation supports the idea that *At*MLKL3 is a bona fide homolog of vertebrate MLKLs despite the low overall amino acid identities between *Arabidopsis* and vertebrate MLKLs in their HeLo (9%–11%) and pseudokinase domains (23%–25%) (Figure 1B). Nevertheless, compared with mMLKL (Murphy et al., 2013), the HeLo domain of *At*MLKL3 packs tightly against its pseudokinase domain (Figure S2D). The packing is further strengthened by the brace region of *At*MLKL3, which contains a string of five helices that simultaneously interact with the HeLo and pseudokinase domains (Figure S2C). The HeLo domains and the brace regions form the core of the *At*MLKL3 tetramer, whereas the pseudokinase domains are arranged at the apices of the pyramid-like structure (Figure 2C). Hydrophobic packing of α1 helices (Figure S2E) from two *At*MLKL3 molecules contributes to formation of a homodimeric *At*MLKL3. In the tetrameric *At*MLKL3, the two α1-mediated homodimers pack perpendicularly to each other (Figure 3C). Four brace regions, which are positioned nearly in
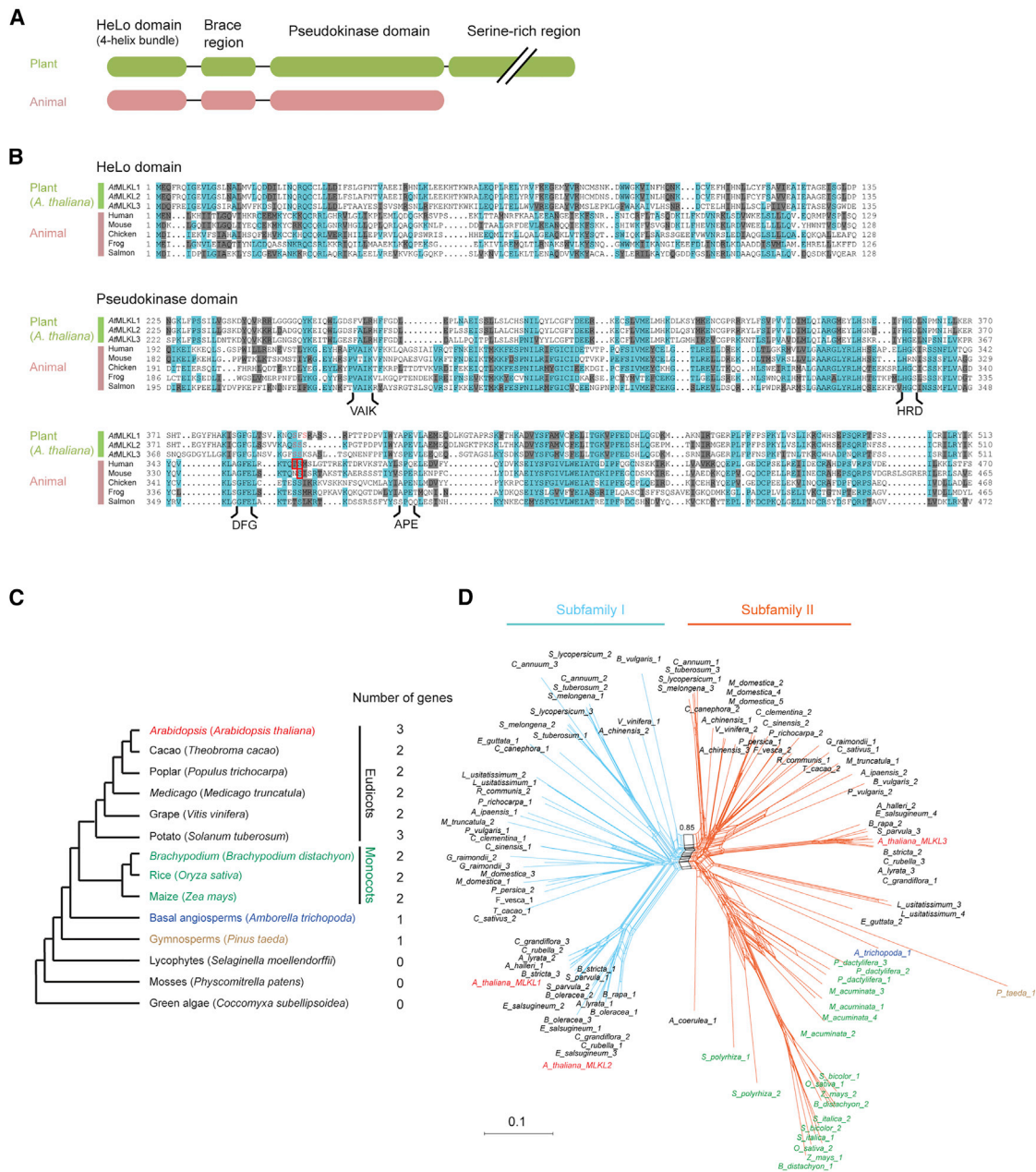
Figure 1. Plant Genomes Encode Proteins that Resemble Animal MLKL

(A) A diagram of plant and animal MLKLs. A variably sized serine-rich region that has no similarity to known structures is directly C-terminal to the pseudokinase domain of plant MLKLs.

(B) Alignments of the four-helix bundles (HeLo domain) and the pseudokinase domains of *A. thaliana* MLKLs (*At*MLKLs) and representative vertebrates. Invariant residues and conservative substitutions in > 50% of the sequences are shown in light blue and gray backgrounds, respectively. The residues responsible for the activation of human or mouse MLKL upon phosphorylation are indicated in the red box. The serine residues examined in this study are shown in red.

(C) Plant MLKL-encoding genes across representative plant species. A full list of MLKL-encoding genes in the genomes of 48 seed plants is shown in Table S1.

(D) Phylogenetic relationship of plant MLKLs. Neighbor-net analysis discriminates two subfamilies of plant MLKLs colored in light blue and orange with a bootstrap support of 0.85 (1,000 bootstrap replicates).

the same plane, are sandwiched between the two homodimers and exclusively mediate homodimer-homodimer interaction (Figure 3D). The N-terminal halves of the four brace regions form two homodimer pairs, and the C-terminal halves form another two pairs (Figure S2E). These intermolecular interactions lead to further sequestration of the *At*MLKL3 N-terminal HeLo domain. Taken together, our observations indicate that *At*MLKL3 structurally resembles vertebrate MLKLs, and its N-terminal HeLo domain is sequestered through both intra- and intermolecular interactions.
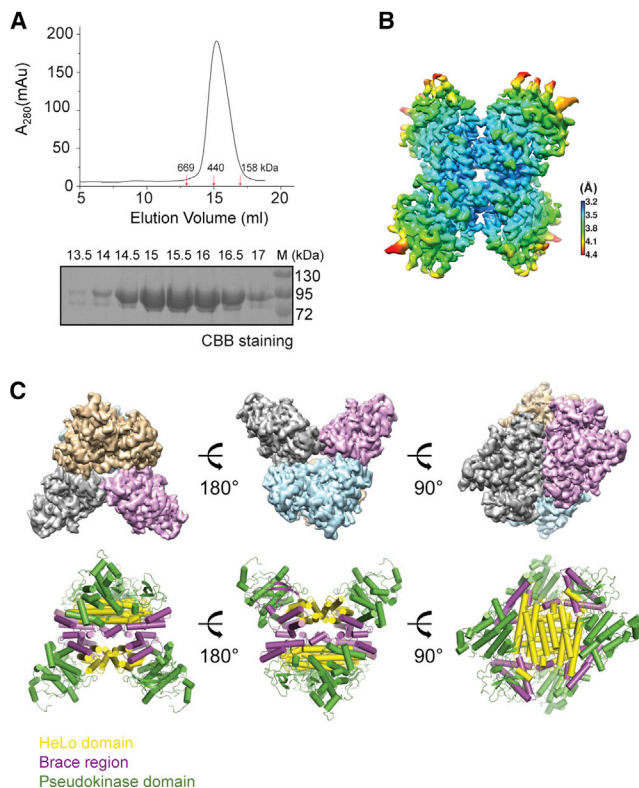
Figure 2. Structure of the *At*MLKL3 Tetramer

(A) Top: gel filtration profiles of *At*MLKL3. Positions of molecular weight standards are indicated by arrows. Bottom: purity of *At*MLKL3 in fractions from the peak shown in the top panel were verified by reducing SDS-PAGE with Coomassie blue staining.

(B) Local resolution (in Å) of the *At*MLKL3 tetramer electron density map. The key to the color scheme scale is shown on the right.

(C) Top: final 3D reconstruction of the *At*MLKL3 tetramer shown in three orientations. Each monomer of *At*MLKL3 is shown in different colors. Bottom: The cartoon shows the overall structure of the *At*MLKL3 tetramer in three orientations. Subdomains of *At*MLKL3 are shown in different colors.

Innate Immunity Function of Plant MLKLs

To determine the role of plant MLKLs in immunity, we challenged combinatorial loss-of-function mutants of *At*MLKLs (Figure S3) with different microbial pathogens. *Atmlkl* single mutants exhibited increased susceptibility to the obligate biotrophic fungus *Golovinomyces orontii* compared with wild-type plants, and, strikingly, the triple mutant was as susceptible as an *eds1* mutant (Figure 4A), which is hyper-susceptible to a number of pathogens (Falk et al., 1999). *Golovinomyces* growth in *A. thaliana* accession Col-0 plants is restricted by an immune response that is not associated with host cell death (Wang et al., 2009). In wild-type Col-0, immunity to the obligate biotrophic oomycete *Hyaloperonospora arabidopsidis* (*Hpa*) race Emwa1, but not *Hpa* race Noco2, and immunity to hemi-biotrophic *Pseudomonas syringae* pv. *tomato* DC3000 bacteria (*Pst* DC3000) carrying *AvrRps4* is mediated by TNLs, RPP4, and RRS1-RPS4, respectively (van der Biezen et al., 2002). RPP4-mediated disease resistance was compromised in the *Atmlkl* triple mutant, as measured by increased *Hpa* spore formation on true leaves (Figure 4B). Similarly, RRS1-RPS4-mediated immunity to *Pst* DC3000 ex-

pressing *AvrRps4* was also compromised in the *Atmlkl* triple mutant (Figure 4C). However, we did not detect marked differences between the susceptibility of wild type and the *Atmlkl* triple mutant plants to *Pst* DC3000 expressing *AvrRpt2* or *AvrRpm1* (Figure 4C), indicating that *At*MLKLs contribute to signaling by TNLs but not CNLs such as RPS2 and RPM1 (Bent et al., 1994; Grant et al., 1995). Immunity to the fungus *Botrytis cinerea* (Figure 4D) and RPS4- and RPM1-mediated host cell death were largely retained in the *Atmlkl123* mutant (Figure 4E).

To determine whether the role of *At*MLKLs in disease resistance is reflected in patterns of gene expression, we performed RNA-seq analysis using mock and *G. orontii*-challenged leaves of wild type, *Atmlkl23*, *Atmlkl123*, and *eds1* lines (Figure 4F). A principal component analysis (PCA) showed that patterns of global gene expression in the *Atmlkl23* and *Atmlkl123* lines overlapped with each other but were distinct from the patterns of wild-type lines (Figure 4F). Instead, they were positioned closer to those of *eds1* especially in mock conditions (Figure 4F). A comparison of the transcriptional changes between wild-type lines and *Atmlkl123* identified 93 differentially expressed genes ($|log_2FC|>1$ and false discovery rate (FDR) < 0.05, Figure S4). This relatively small number of differentially expressed genes might be attributed to the suppression of immune signaling by *G. orontii* that is partly adapted to this host plant (Plotnikova et al., 1998). In accordance with the PCA analysis, the expression profile of a subset of the 93 genes was similar in *Atmlkl123* and *eds1* lines (Figure S4). The gene ontology term response to biotic or abiotic stresses (GO:0006950) was overrepresented in the downregulated genes in *Atmlkl123* compared with wild-type lines (Figure S4). These data imply a partly overlapping role of *At*MLKLs and EDS1 in shaping gene expression under both unchallenged conditions and in the presence of a pathogen.

Cell Death Activity of Plant MLKLs

Phosphorylation in the activation loop of the pseudokinase domain is an initial step in MLKL-dependent necroptosis in animals (Petrie et al., 2019; Vanden Berghe et al., 2014). To test whether *At*MLKLs possess cell death activity, possibly regulated by phosphorylation, we introduced single phosphomimetic substitutions at serine residues in the activation loops of *At*MLKLs (Figure 1B) and expressed the variants in *A. thaliana* leaf protoplasts (Figure S5, see the STAR Methods section). Upon overexpression, all wild-type *At*MLKLs elicited cell death, which was as potent as an N-terminal barley NLR cell death module (Jacob et al., 2018; Figure S5B). We found that a phosphomimetic substitution at serine[393] (S393D) but not serine[395] (S395D) in *At*MLKL1 enhanced its cell-killing activity (Figure 5A). Interestingly, a phosphoablating substitution at serine[393] (S393A) also enhanced the cell death activity (Figure S5D). Using transgenic *A. thaliana* lines, we observed that the enhanced susceptibility of *Atmlkl1* and *Atmlkl2* mutants to *G. orontii* was complemented by stable transformations of genomic fragments encompassing wild-type *AtMLKL1* and *AtMLKL2*, respectively (Figures 5B, 5C, and S6). In line with the protoplast assay (Figure 5A), *At*MLKL1 (S393D) transgenic plants exhibited enhanced resistance to *G. orontii* compared with wild-type Col-0 or plants expressing *AtMLKL1* or *AtMLKL1* (S395D) transgenes (Figures 5B and 5C). Unexpectedly, *AtMLKL1* (S393D) transgenic plants did not exhibit cell death lesions or apparent plant growth retardation indicative of autoimmunity (Figures 5B and S6A). An independent
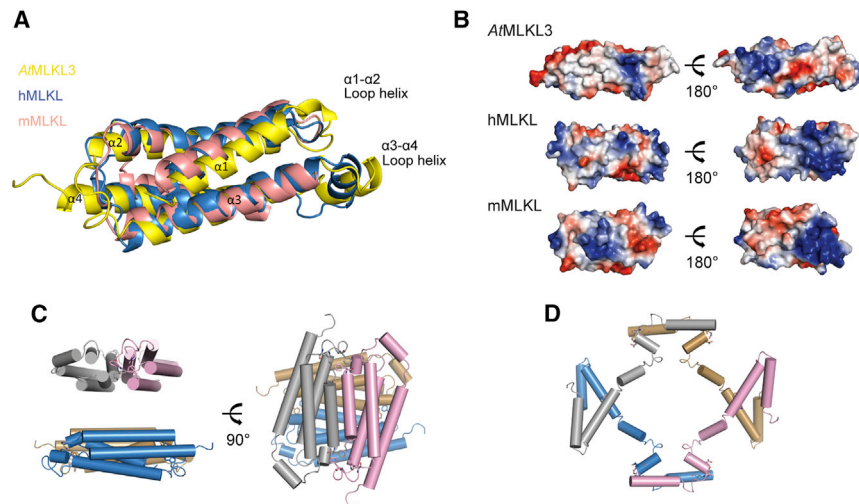
Figure 3. Structure of the HeLo Domains of AtMLKL3

(A) Superposition of the HeLo domains of AtMLKL3 (yellow, PDB ID code 6KA4), human MLKL (blue, PDB ID code 2MSV), and mouse MLKL (pink, PDB ID code 4BTF). RMSD between AtMLKL3 and mMLKL:3.745 Å, RMSD between AtMLKL3 and hMLKL: 4.010 Å.

(B) Electrostatic surface of HeLo domains of AtMLKL3, human MLKL and mouse MLKL in two orientations. Deep blue represents positively charged and red represents negatively charged areas.

(C) A cartoon showing the HeLo domains of the AtMLKL3 tetramer in two orientations. Monomers of AtMLKL3 are shown in different colors.

(D) A cartoon showing the brace region of the AtMLKL3 tetramer. Monomers of AtMLKL3 are shown in different colors.

AtMLKL1 (S393D) transgenic plant also exhibited enhanced resistance to *G. orontii* (Figure 5C). Collectively, these data show that AtMLKL1 activity needed to restrict *G. orontii* growth can be separated from host cell death.

We next examined whether the AtMLKL N-terminal HeLo domain contributes to its cell death activity, as in animals (Hildebrand et al., 2014; Petrie et al., 2019; Quarato et al., 2016; Tanzer et al., 2016). Taking advantage of a chemically enforced oligomerization system (Figure 6A, see the STAR Methods section), we found that expression of the HeLo domains with the brace region of AtMLKL1 and AtMLKL3 was sufficient for cytotoxic activity, and this activity was further enhanced upon oligomerization (Figure 6B). This finding mirrors the activity of the HeLo domains with the brace region of MLKL (Quarato et al., 2016; Tanzer et al., 2016) and is consistent with our structure-informed hypothesis that the full-length MLKL tetramer with buried HeLo domains (Figure 2) represents an inactive form.

Intracellular Localization and Disease Resistance Activities of Plant MLKLs

As MLKLs translocate to the plasma membrane upon activation (Chen et al., 2014; Dondelinger et al., 2014; Hildebrand et al., 2014; Petrie et al., 2020; Quarato et al., 2016; Wang et al., 2014; Samson et al., 2020), we examined whether GFP-tagged AtMLKL1 variants, in the *Atmlkl1* complementation line (Figures 5B, 5C, and S6A), associate with the plasma membrane using time-resolved confocal microscopy. We detected mobile punctate signals in the cytoplasmic space for all AtMLKL1 variants (Figures 7A and 7B). We observed reduced mobility for a fraction of AtMLKL1-GFP signals when proximal to the plasma membrane (Figures 7A and 7B; Videos S1, S2, and S3), which is consistent with plasma membrane association. Intriguingly, maximum projection of the time-lapse images revealed that AtMLKL1 (wild type)-GFP and AtMLKL1 (S395D)-GFP mutant but not AtMLKL1 (S393D)-GFP moved along filamentous structures (Figure 7B; Videos S1, S2, and S3). Filamentous structures were also undetectable in the second independent AtMLKL1 (S393D) transgenic plant (Figure S6F). The GFP- and YFP-tagged AtMLKL1 filaments specifically colocalized with the microtubule markers mCherry-

MAP4 (Figures S7A–S7C) and mCherry-TUB6 (Figure 7C) (Marc et al., 1998), and association was detectable upon *G. orontii* invasion (Figure S7E). No filamentous movement was detected in the S393D phosphomimetic line despite the presence of a microtubule array (Figure 7C; projected over time), although this variant with the YFP-tag was still able to associate with microtubules in protoplasts upon overexpression (Figure 7D; a single slice snapshot). These data suggest that the phosphomimetic mutation modulates intracellular localization and dynamics of AtMLKL1, which are both linked with cytoskeletal association.

To gain further insight into the intracellular localization and functions of plant MLKLs upon perception of conserved microbial patterns by cell surface receptors, we examined AtMLKL1-GFP mobility upon exposure to chitin, a fungal-derived PAMP (Boutrot and Zipfel, 2017). For this, we used hypocotyls of plants grown in the dark, in which we obtained a high signal-to-noise GFP fluorescence ratio, and a mixture of chitin oligomers (NA-COS-Y) or a chitin heptamer ([GlcNAc]$_7$). We recorded a high variation in the dwell time of AtMLKL1-GFP particles at specific loci within and between independent hypocotyl cells (Figure S7F, see the STAR Methods section). However, the overall distribution of the AtMLKL1-GFP dwell time was prolonged when cells were treated with either form of chitin (Figure 7E). Notably, the proportion of highly mobile particles (those staying no longer than two frames at a given locus) to immobile particles significantly declined in chitin-treated cells (Figure 7F), illustrating the ability of AtMLKL1-GFP to respond to chitin signals and alter its subcellular dynamics from a mobile to an immobile state. Combined with the inability of the AtMLKL1(S393D)-GFP phosphomimetic variant to move along microtubules (Figures 7B and 7C), although it retains association with these structures (Figure 7D), our findings suggest a model in which the immobilization of AtMLKL proteins in response to recognition of fungal pathogens triggers an immune response leading to the restriction of fungal invasion.

DISCUSSION

We report the discovery of a protein family in seed plants that structurally and functionally resembles animal MLKL. Our study
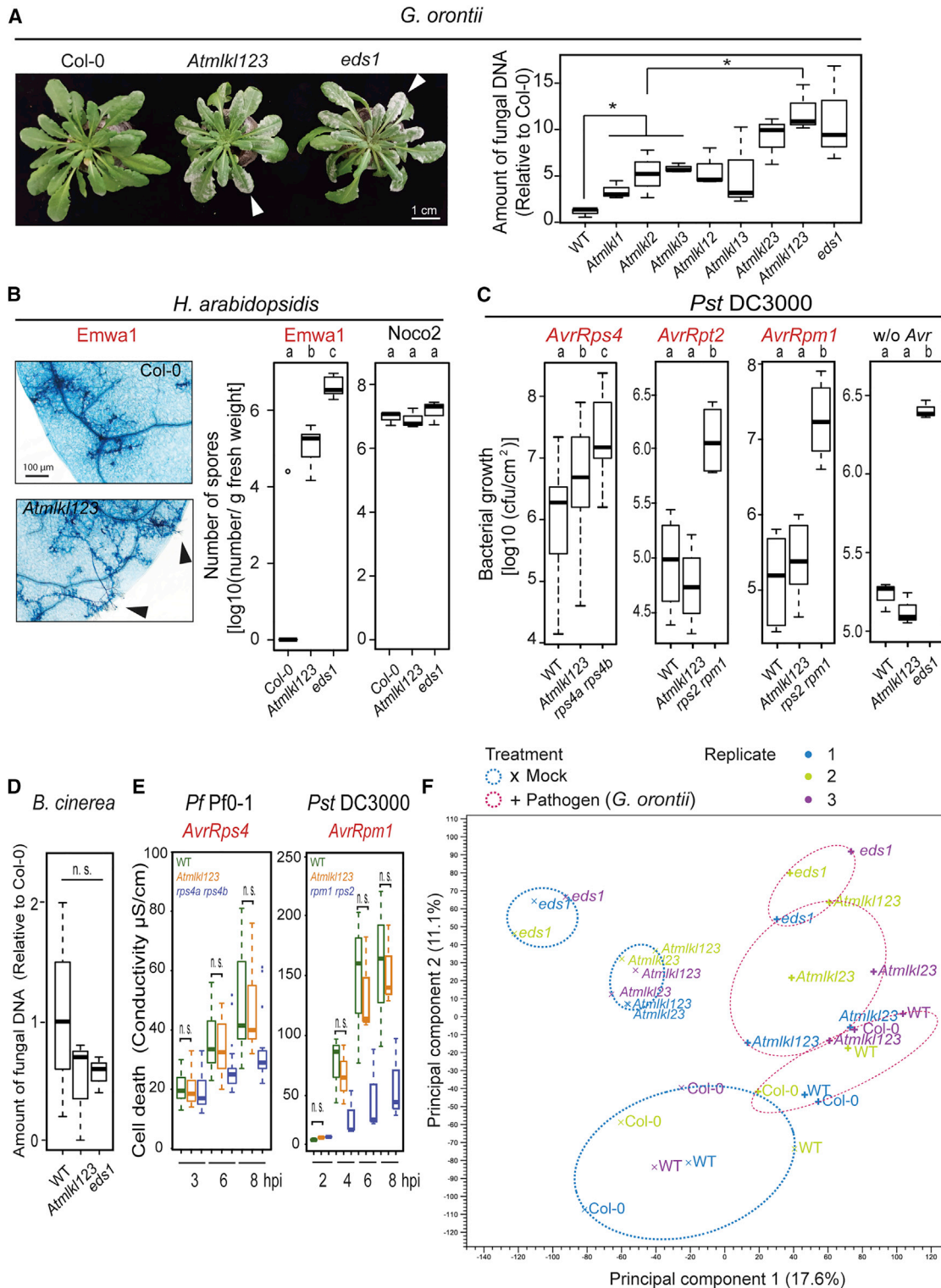
Figure 4. Arabidopsis MLKLs Confer Resistance to Biotrophic Fungal, Oomycetal, and Bacterial Pathogens

(A) *Atmlkl* mutants are susceptible to the powdery mildew *Golovinomyces orontii* (arrowheads). Quantification of *G. orontii* DNA at seven days after inoculation is relative to the corresponding Col-0 samples. (n = 3, Tukey HSD *p < 0.05).

(B) The *Atmlkl* triple mutant is susceptible to the downy mildew *Hyaloperonospora arabidopsidis* race Emwa1 (n = 6) but not Noco2 (n = 3). The 1st or 2nd true leaves were stained with trypan blue to visualize hyphal growth. Sporangiophores were formed on the true leaves of the *Atmlkl* triple mutant (black arrowheads).
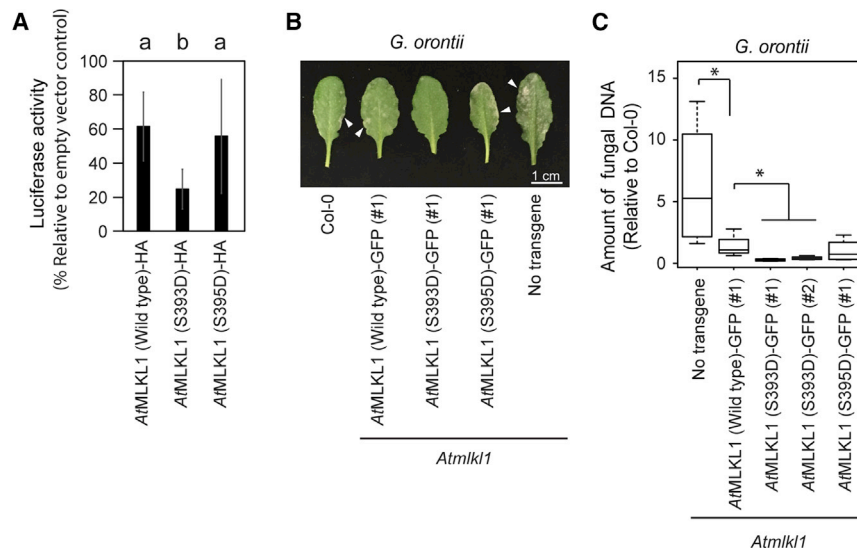
Figure 5. Cell Death Activity and Disease Resistance of Phosphomimetic *At*MLKL1 Variants

(A) A phosphomimetic substitution in *At*MLKL1 elicited enhanced cell death in *Arabidopsis* mesophyll protoplasts isolated from Col-0. Luciferase and *At*MLKL1 expression constructs were co-transfected into protoplasts and luciferase activity was measured as a proxy for cell viability at 16 h post-transfection. The positions of serine-to-aspartate substitutions are indicated in Figure 1B. The C-terminally HA-tagged variants were expressed under the control of the constitutive cauliflower mosaic virus 35S promoter. (n = 3, Tukey HSD *p < 0.01) Error bars indicate standard deviation.

(B) Macroscopic phenotype of transgenic *Arabidopsis* expressing phosphomimetic variants of *At*MLKL1 in response to *G. orontii* (arrowheads). Plants were photographed seven days after pathogen challenge.

(C) Quantification of *G. orontii* DNA in infected leaves of transgenic plants at 14 days after pathogen challenge is relative to the corresponding Col-0 samples (n = 4, Tukey HSD *p < 0.05).

also provides experimental evidence for evolutionary conservation of the HeLo domain fold in animals and plants.

Our structural and biochemical data showed that the HeLo domain is completely sequestered in the tetrameric *At*MLKL2 and *At*MLKL3 through intra- and intermolecular interactions (Figures 2, S2C, and S2E). This contrasts with the monomeric mouse MLKL structure (Murphy et al., 2013; Figure S2D) or tetrameric human MLKL (Petrie et al., 2018) in which these domains are exposed. Interestingly, however, sequestration of the HeLo domain in *At*MLKLs, which is important for signaling, is reminiscent of autoinhibition of the CC domain of ZAR1 CNL in its resting state (Wang et al., 2019), although ZAR1 employs a different mechanism for CC domain inhibition. These results suggest that the structures of *At*MLKL2 and *At*MLKL3 observed in our study represent inactive states. Consistently, overexpression of the HeLo domains with the brace linker regions of *At*MLKL1,3 elicited cell death (Figure 6B). It is conceivable that the pseudokinase domain of *At*MLKLs has an important role in activation as seen for animal MLKL (Hildebrand et al., 2014; Petrie et al., 2019). In agreement with this idea, mutations in the activation loop of *At*MLKL1 resulted in enhanced resistance to powdery mildew pathogen (Figure 5). Given that the activation loop is located far away from the HeLo domain in the tetrameric *At*MLKL2 and 3, this suggests that modifications of this portion of the pseudokinase domain may function to allosterically relieve

the autoinhibition of *At*MLKLs, leading to exposure of the HeLo domain. As the HeLo domain with brace linker region of *At*MLKLs exhibited cell death-inducing activity that was further potentiated by enforced oligomerization (Figure 6B), it is possible that *At*MLKL-mediated signaling involves a tetrameric form of *At*MLKLs, in which oligomerized HeLo domains initiate downstream signaling. Future studies directed at how the autoinhibition is relieved should facilitate our understanding of *At*MLKL-mediated immune signaling.

We showed that *At*MLKLs are preferentially engaged by the TNL- but not CNL-triggered immune machinery (Figures 4B and 4C). TIR-like domains were recently shown to have an enzymatic activity that cleaves NAD$^+$ (nicotinamide adenine dinucleotide) (Horsefield et al., 2019; Wan et al., 2019). A current model proposes that products generated by NAD$^+$ cleavage act as signaling molecules for RNL-dependent signaling downstream of TNL-triggered immunity (Horsefield et al., 2019; Wan et al., 2019). Thus, plant MLKLs and RNLs might be activated by the same NAD$^+$ -derived signal. We propose that the observed hyper-susceptibility of the *Atmlkl123* mutant to *G. orontii* (Figure 4A) might be due to compromised immune signaling mediated by weak and yet unknown TNL receptor(s).

Both phosphomimetic and phosphoablating substitutions of serine[393] in the activation loop of *At*MLKL1 elicited enhanced cell death in *Arabidopsis* mesophyll protoplasts (Figures 5A

(C) The *Atmlkl* triple mutant is susceptible to the *Pseudomonas syringae* pv. tomato DC3000 (*Pst* DC300) strain expressing *AvrRps4* avirulent effector (n = 36) but not to strains expressing *AvrRpt2* (n = 4), *AvrRpm1* (n = 6) or without avirulent effectors (w/o *Avr*, n = 3).

(B and C) Avirulent race of *Hpa* and *Pst* effectors are indicated in red. Different letters indicate significant differences (Tukey HSD p < 0.05).

(D) *Arabidopsis* MLKLs do not confer resistance to a necrotrophic fungal pathogen. *Botrytis cinerea* DNA was quantified by qPCR at three days after spore inoculation and normalized to the amount of a plant-specific gene (see the STAR Methods section). Amounts are presented relative to the corresponding Col-0 samples (n = 3).

(E) *Arabidopsis* MLKLs are not essential for host cell death in response to avirulent bacterial pathogens. Ion leakage assay in *A. thaliana* leaves upon infiltration with the indicated bacterial strain expressing *AvrRPS4* (n = 18) and the *AvrRpm1* (n = 3). n.s., not significant.

(F) Principal component analysis (PCA) of RNA-seq data from mock- and pathogen-challenged leaves collected at 48 h post *G. orontii* inoculation.

*WT (wild type) is a segregant line derived from the cross between *Atmlkl1* and *Atmlkl3*. The *eds1* mutant was used as a susceptible control.
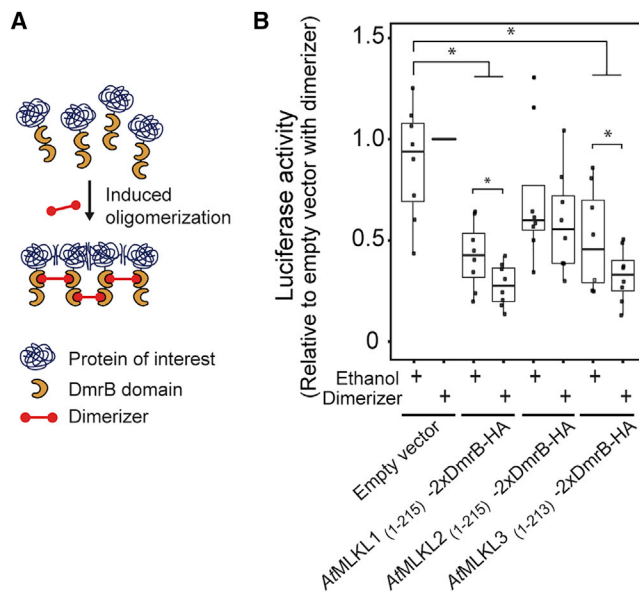
A

B

Figure 6. The HeLo Domain Plus Brace Region of *At*MLKL1 and *At*MLKL3 Were Sufficient to Elicit Cell Death

(A) Schematic diagram of chemically induced oligomerization. AP20187 (Dimerizer), a synthetic cell-permeable ligand, induces homodimerization of fusion proteins containing the DmrB domain. Dimerizer-dependent oligomerization is facilitated by a tandem fusion of DmrB domains.

(B) Enforced oligomerization of the HeLo domain plus brace region of *At*MLKL1 and *At*MLKL3 potentiated their activities. Expression constructs for luciferase and each of the *At*MLKL fusion proteins indicated in the figure were co-transfected into protoplasts, and luciferase activity was measured as a proxy of cell viability at 16 h post-transfection. Relative luciferase activities compared with those of the empty vector control with dimerizer are plotted. Data were obtained with eight independent transfections (n = 9). Asterisks indicate statistically significant differences (Tukey HSD, *p < 0.01). Mesophyll protoplasts were isolated from the triple mutant *Atmlkl123* and AP20187 (dimerizer) was added after transfection (see the STAR Methods section).

and S5D), suggesting that plant MLKL function is in part regulated by activation loop conformation. Therefore, we do not exclude the possibility that post-translational modifications other than phosphorylation mediate a conformational change in the activation loop of plant MLKLs. This might explain the finding that, unlike *At*MLKL1, single phosphomimetic substitutions in the activation loops of *At*MLKL2 and 3 did not elicit enhanced cell death (Figure S5C). It is possible that the thresholds or types of conformational changes in the activation loops are different between the three *At*MLKLs, as the activation loop sequences diverge between *At*MLKL1-3 (Figure 1B).

Plant microtubules form a highly ordered non-centrosomal array immediately beneath the plasma membrane, and microtubules are proposed to be involved in timely deployment of proteins to the plasma membrane (Oda, 2018). In this study, we found that a fraction of *At*MLKL1 and *At*MLKL2 associates with microtubules, while a fraction of *At*MLKL1 is less mobile when proximal to the plasma membrane (Figure 7B; Videos S1, S2, and S3). Only recently, microtubules were attributed a role in translocating animal MLKL from cytoplasmic necrosomes to the plasma membrane, where membrane disruption causes cell death (Samson et al., 2020). Previous studies

in plants have demonstrated that the integrity of microtubule organization is important for resistance to pathogens (Hoefle et al., 2011), supported by the fact that several pathogens deliver effector proteins into host cells to perturb microtubule organization (Guo et al., 2016; Lee et al., 2012). Therefore, microtubule-associated *At*MLKLs might enable a rapid response to perturbation of microtubule organization caused by pathogens. An *At*MLKL1 phosphomimetic variant (S393D) exhibited reduced microtubule mobility (Figures 7B–7D) and enhanced resistance to the powdery mildew pathogen (Figures 5B and 5C), but this variant did not impair plant growth (Figure S6A), indicating that this *At*MLKL1 variant is not constitutively active. Importantly, *At*MLKL1 mobility was slowed in response to chitin, a fungal-derived PAMP (Figures 7E and 7F). Thus, a less mobile *At*MLKL fraction appears to reflect a primed resistance state that allows plants to execute stronger defense responses when challenged with a pathogen (Martinez-Medina et al., 2016). For transition from the primed resistance state to a full-activation state, plant MLKLs would likely require additional cue(s) such as the above-discussed NAD$^+$-derived signal generated by TNLs.

The plant MLKL family described here is an example of a non-receptor immune system component consisting of multiple domains that is structurally shared between animals and plants. It will be intriguing to determine whether animal and plant MLKLs and other HeLo domain-containing proteins share a common biochemical mechanism involving the formation of pores or pore-like structures at the plasma membrane, ultimately leading to cell death and/or immunity. Our work serves as a basis to test structural predictions implicating the presence of a HeLo domain fold in a number of plant modular proteins, including the ADR1 and NRG1 families of RNLs (Barragan et al., 2019; Bentham et al., 2018; Daskalov et al., 2016; Jubic et al., 2019). Although the putative HeLo domain of the ADR1 family harbors cell death activity (Collier et al., 2011), ADR1 family proteins confer disease resistance without apparent host cell death (Bonardi et al., 2011). This resembles the immune response of wild-type plants to *G. orontii*, which is mediated by *At*MLKL in the absence of host cell death, although these proteins have the capacity to elicit cytotoxicity. Therefore, it is intriguing to know whether and how the cell death activity of MLKLs is linked to the *At*MLKL-mediated immunity. These results also raise the question of whether host defense and cell death functions can be further disentangled in animal necroptosis signaling.

STAR★METHODS

Detailed methods are provided in the online version of this paper and include the following:

- KEY RESOURCES TABLE
- RESOURCE AVAILABILITY
  - Lead Contact
  - Materials Availability
  - Data and Code Availability
- EXPERIMENTAL MODEL AND SUBJECT DETAILS
  - Plant Material and Growth Conditions
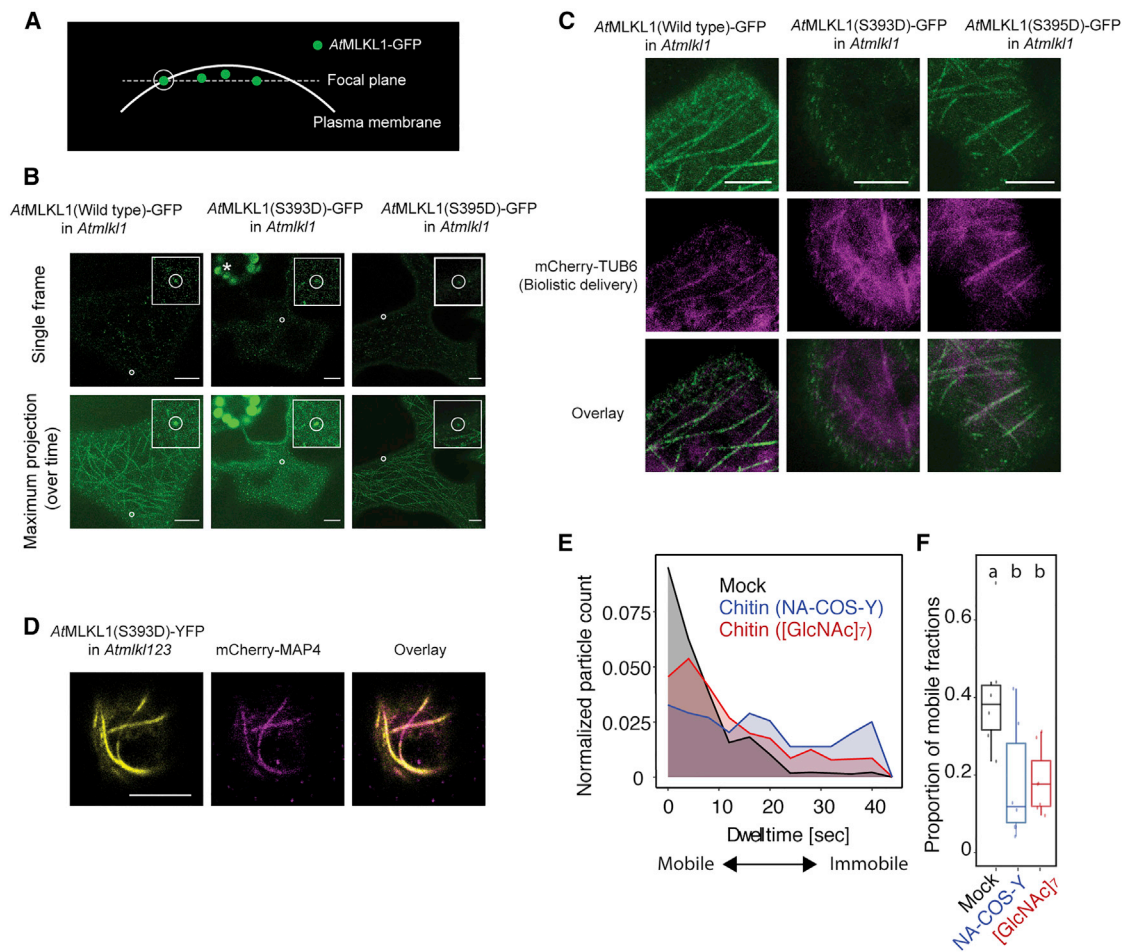 - Bacterial Strains
- METHOD DETAILS

Figure 7. Intracellular Localization of *At*MLKL1

(A) Schematic diagram of the confocal images shown in (B). The white circle indicates GFP signal proximal to the plasma membrane.

(B) Confocal images of the abaxial epidermis of the *Arabidopsis* transgenic lines expressing phosphomimetic and wild-type variants of *At*MLKL1. GFP signals indicated by white circles were immobile in the examined time period. The corresponding movies are available as Videos S1, S2, and S3. Three times magnified images of immobile signals were shown in each inlet. The asterisk indicates plastidial autofluorescence. Scale bars, 5 μm.

(C) Cortical microtubule arrays in abaxial leaf epidermal cells of transgenic *A. thaliana* lines expressing phosphomimetic and wild-type variants of *At*MLKL1. Representative images were obtained one day after biolistic delivery of the expression construct for the *At*ubiquitin10 promoter driven by mCherry-TUB6 (microtubule marker; Fujita et al., 2013) into the indicated transgenic lines. Scale bars, 5 μm.

(D) Subcellular localization of the *At*MLKL1 S393D variant in *Arabidopsis* mesophyll protoplasts isolated from *Atmlkl123*. Representative confocal images were taken at 10 h post-transfection. Scale bar, 10 μm.

(E) Density plot of the *At*MLKL1-GFP dwell time in hypocotyl cells treated with NA-COS-Y, a mixture of chitin oligomers or $[GlcNAc]_7$, a chitin heptamer (blue and red, respectively), compared with mock-treated control cells (black), calculated from the time series images over 50 frames with 0.82-s intervals.

(F) Quantification of the "mobile fraction," i.e., particles that did not stay longer than two frames in the beginning of the acquired images. Letters indicate statistical significance corresponding to Tukey's HSD test (n = 19; $p < 0.05$).

○ Sequence Analysis of Plant and Animal MLKLs
○ Protein Expression and Purification
○ Cryo-EM Analysis
○ Image Processing and 3D Reconstruction
○ Model Building and Refinement
○ RNA Sequencing
○ Transient Gene Expression in Protoplasts
○ Protoplast Viability Assay
○ Induced Oligomerization
○ Pathogen Infection Assays
○ Immunoblot Assays
○ Biolistic Transient Gene Expression

○ Confocal Microscopy
○ Chitin Treatment and Image Analysis
● QUANTIFICATION AND STATISTICAL ANALYSIS

AUTHOR CONTRIBUTIONS

T.M. conceptualized the project; L.M., M.H., X.Z., R.T.N., L.B.K., I.M.L.S., F.J., V.K., D.L., K.H., and T.M. performed the investigations; J.E.P., J.M.M., P.S.-L., J.C., and T.M. validated the data; J.E.P., J.M.M., P.S.-L., J.C., and T.M. supervised the work; J.C. and T.M. wrote the original draft of the manuscript; J.E.P., P.S.-L., and J.M.M. reviewed and edited the manuscript.

DECLARATION OF INTERESTS

The authors declare no competing interests.

SUPPORTING CITATIONS

The following references appear in the Supplemental Information: Riedl et al., 2008, Rosso et al., 2003.

REFERENCES

Aarts, N., Metz, M., Holub, E., Staskawicz, B.J., Daniels, M.J., and Parker, J.E. (1998). Different requirements for EDS1 and NDR1 by disease resistance genes define at least two R gene-mediated signaling pathways in Arabidopsis. Proc. Natl. Acad. Sci. USA 95, 10306–10311.

Adams, P.D., Afonine, P.V., Bunkóczi, G., Chen, V.B., Davis, I.W., Echols, N., Headd, J.J., Hung, L.W., Kapral, G.J., Grosse-Kunstleve, R.W., et al. (2010). PHENIX: a comprehensive Python-based system for macromolecular structure solution. Acta Crystallogr. D Biol. Crystallogr. 66, 213–221.

Alonso, J.M., Stepanova, A.N., Leisse, T.J., Kim, C.J., Chen, H., Shinn, P., Stevenson, D.K., Zimmerman, J., Barajas, P., Cheuk, R., et al. (2003). Genome-wide insertional mutagenesis of Arabidopsis thaliana. Science 301, 653–657.

Bai, S., Liu, J., Chang, C., Zhang, L., Maekawa, T., Wang, Q., Xiao, W., Liu, Y., Chai, J., Takken, F.L.W., et al. (2012). Structure-function analysis of barley NLR immune receptor MLA10 reveals its cell compartment specific activity in cell death and disease resistance. PLoS Pathog. 8, e1002752.

Barragan, C.A., Wu, R., Kim, S.T., Xi, W., Habring, A., Hagmann, J., Van de Weyer, A.L., Zaidem, M., Ho, W.W.H., Wang, G., et al. (2019). RPW8/HR repeats control NLR activation in Arabidopsis thaliana. PLoS Genet. 15, e1008313.

Bartsch, M., Gobbato, E., Bednarek, P., Debey, S., Schultze, J.L., Bautor, J., and Parker, J.E. (2006). Salicylic acid-independent ENHANCED DISEASE SUSCEPTIBILITY1 signaling in Arabidopsis immunity and cell death is regulated by the monooxygenase FMO1 and the Nudix hydrolase NUDT7. Plant Cell 18, 1038–1051.

Bendahmane, A., Kanyuka, K., and Baulcombe, D.C. (1999). The Rx gene from potato controls separate virus resistance and cell death responses. Plant Cell 11, 781–792.

Bent, A.F., Kunkel, B.N., Dahlbeck, D., Brown, K.L., Schmidt, R., Giraudat, J., Leung, J., and Staskawicz, B.J. (1994). RPS2 of Arabidopsis thaliana: a leucine-rich repeat class of plant disease resistance genes. Science 265, 1856–1860.

Bentham, A.R., Zdrzalek, R., De la Concepcion, J.C., and Banfield, M.J. (2018). Uncoiling CNLs: structure/function approaches to understanding CC domain function in plant NLRs. Plant Cell Physiol. 59, 2398–2408.

Birkenbihl, R.P., Diezel, C., and Somssich, I.E. (2012). Arabidopsis WRKY33 is a key transcriptional regulator of hormonal and metabolic responses toward Botrytis cinerea infection. Plant Physiol. 159, 266–285.

Bonardi, V., Tang, S., Stallmann, A., Roberts, M., Cherkis, K., and Dangl, J.L. (2011). Expanded functions for a family of plant intracellular immune receptors beyond specific recognition of pathogen effectors. Proc. Natl. Acad. Sci. USA 108, 16463–16468.

Boutrot, F., and Zipfel, C. (2017). Function, discovery, and exploitation of plant pattern recognition receptors for broad-spectrum disease resistance. Annu. Rev. Phytopathol. 55, 257–286.

Brown, A., Long, F., Nicholls, R.A., Toots, J., Emsley, P., and Murshudov, G. (2015). Tools for macromolecular model building and refinement into electron cryo-microscopy reconstructions. Acta Crystallogr. D Biol. Crystallogr. 71, 136–153.

Bucher, P., Karplus, K., Moeri, N., and Hofmann, K. (1996). A flexible motif search technique based on generalized profiles. Comput. Chem. 20, 3–23.

Cabral, A., Stassen, J.H., Seidl, M.F., Bautor, J., Parker, J.E., and Van den Ackerveken, G. (2011). Identification of Hyaloperonospora arabidopsidis transcript sequences expressed during infection reveals isolate-specific effectors. PLoS One 6, e19328.

Castel, B., Ngou, P.M., Cevik, V., Redkar, A., Kim, D.S., Yang, Y., Ding, P., and Jones, J.D.G. (2019). Diverse NLR immune receptors activate defence via the RPW8-NLR NRG1. New Phytol. 222, 966–980.

Chan, F.K., Luz, N.F., and Moriwaki, K. (2015). Programmed necrosis in the cross talk of cell death and inflammation. Annu. Rev. Immunol. 33, 79–106.

Chen, X., Li, W., Ren, J., Huang, D., He, W.T., Song, Y., Yang, C., Li, W., Zheng, X., Chen, P., and Han, J. (2014). Translocation of mixed lineage kinase domain-like protein to plasma membrane leads to necrotic cell death. Cell Res. 24, 105–121.

Clough, S.J., and Bent, A.F. (1998). Floral dip: a simplified method for Agrobacterium-mediated transformation of Arabidopsis thaliana. Plant J. 16, 735–743.

Coll, N.S., Epple, P., and Dangl, J.L. (2011). Programmed cell death in the plant immune system. Cell Death Differ. 18, 1247–1256.

Coll, N.S., Vercammen, D., Smidler, A., Clover, C., Van Breusegem, F., Dangl, J.L., and Epple, P. (2010). Arabidopsis type I metacaspases control cell death. Science 330, 1393–1397.

Collier, S.M., Hamel, L.P., and Moffett, P. (2011). Cell death mediated by the N-terminal domains of a unique and highly conserved class of NB-LRR protein. Mol. Plant Microbe Interact. 24, 918–931.

Daskalov, A., Habenstein, B., Sabaté, R., Berbon, M., Martinez, D., Chaignepain, S., Coulary-Salin, B., Hofmann, K., Loquet, A., and Saupe, S.J. (2016). Identification of a novel cell death-inducing domain reveals that fungal amyloid-controlled programmed cell death is related to necroptosis. Proc. Natl. Acad. Sci. USA 113, 2720–2725.

Dondelinger, Y., Declercq, W., Montessuit, S., Roelandt, R., Goncalves, A., Bruggeman, I., Hulpiau, P., Weber, K., Sehon, C.A., Marquis, R.W., et al. (2014). MLKL compromises plasma membrane integrity by binding to phosphatidylinositol phosphates. Cell Rep. 7, 971–981.

Falk, A., Feys, B.J., Frost, L.N., Jones, J.D., Daniels, M.J., and Parker, J.E. (1999). EDS1, an essential component of R gene-mediated disease resistance in Arabidopsis has homology to eukaryotic lipases. Proc. Natl. Acad. Sci. USA 96, 3292–3297.

Fujita, S., Pytela, J., Hotta, T., Kato, T., Hamada, T., Akamatsu, R., Ishida, Y., Kutsuna, N., Hasezawa, S., Nomura, Y., et al. (2013). An atypical tubulin kinase mediates stress-induced microtubule depolymerization in Arabidopsis. Curr. Biol. *23*, 1969–1978.

Gachon, C., and Saindrenan, P. (2004). Real-time PCR monitoring of fungal development in Arabidopsis thaliana infected by Alternaria brassicicola and Botrytis cinerea. Plant Physiol. Biochem. *42*, 367–371.

Gehl, C., Kaufholdt, D., Hamisch, D., Bikker, R., Kudla, J., Mendel, R.R., and Hänsch, R. (2011). Quantitative analysis of dynamic protein-protein interactions in planta by a floated-leaf luciferase complementation imaging (FLuCI) assay using binary Gateway vectors. Plant J. *67*, 542–553.

Grant, M.R., Godiard, L., Straube, E., Ashfield, T., Lewald, J., Sattler, A., Innes, R.W., and Dangl, J.L. (1995). Structure of the Arabidopsis RPM1 gene enabling dual specificity disease resistance. Science *269*, 843–846.

Guo, M., Kim, P., Li, G., Elowsky, C.G., and Alfano, J.R. (2016). A bacterial effector co-opts calmodulin to target the plant microtubule network. Cell Host Microbe *19*, 67–78.

Hamada, T., Nagasaki-Takeuchi, N., Kato, T., Fujiwara, M., Sonobe, S., Fukao, Y., and Hashimoto, T. (2013). Purification and characterization of novel microtubule-associated proteins from Arabidopsis cell suspension cultures. Plant Physiol. *163*, 1804–1816.

Hildebrand, J.M., Tanzer, M.C., Lucet, I.S., Young, S.N., Spall, S.K., Sharma, P., Pierotti, C., Garnier, J.M., Dobson, R.C., Webb, A.I., et al. (2014). Activation of the pseudokinase MLKL unleashes the four-helix bundle domain to induce membrane localization and necroptotic cell death. Proc. Natl. Acad. Sci. USA *111*, 15072–15077.

Hoefle, C., Huesmann, C., Schultheiss, H., Börnke, F., Hensel, G., Kumlehn, J., and Hückelhoven, R. (2011). A barley ROP GTPase activating protein associates with microtubules and regulates entry of the barley powdery mildew fungus into leaf epidermal cells. Plant Cell *23*, 2422–2439.

Horsefield, S., Burdett, H., Zhang, X., Manik, M.K., Shi, Y., Chen, J., Qi, T., Gilley, J., Lai, J.S., Rank, M.X., et al. (2019). NAD+ cleavage activity by animal and plant TIR domains in cell death pathways. Science *365*, 793–799.

Jacob, F., Kracher, B., Mine, A., Seyfferth, C., Blanvillain-Baufumé, S., Parker, J.E., Tsuda, K., Schulze-Lefert, P., and Maekawa, T. (2018). A dominant-interfering camta3 mutation compromises primary transcriptional outputs mediated by both cell surface and intracellular immune receptors in Arabidopsis thaliana. New Phytol. *217*, 1667–1680.

Jacob, F., Vernaldi, S., and Maekawa, T. (2013). Evolution and conservation of plant NLR functions. Front. Immunol. *4*, 297.

Jones, J.D., Vance, R.E., and Dangl, J.L. (2016). Intracellular innate immune surveillance devices in plants and animals. Science *354*, aaf6395.

Jubic, L.M., Saile, S., Furzer, O.J., El Kasmi, F., and Dangl, J.L. (2019). Help wanted: helper NLRs and plant immune responses. Curr. Opin. Plant Biol. *50*, 82–94.

Katoh, K., Misawa, K., Kuma, K., and Miyata, T. (2002). MAFFT: a novel method for rapid multiple sequence alignment based on fast Fourier transform. Nucleic Acids Res. *30*, 3059–3066.

Kleinboelting, N., Huep, G., Kloetgen, A., Viehoever, P., and Weisshaar, B. (2012). GABI-Kat SimpleSearch: new features of the Arabidopsis thaliana T-DNA mutant database. Nucleic Acids Res. *40*, D1211–D1215.

Koncz, C., and Schell, J. (1986). The promoter of TL-DNA gene 5 controls the tissue-specific expression of chimaeric genes carried by a novel type of Agrobacterium binary vector. Mol. Gen. Genet. MGG *204*, 383–396.

Lapin, D., Kovacova, V., Sun, X., Dongus, J.A., Bhandari, D., von Born, P., Bautor, J., Guarneri, N., Rzemieniewski, J., Stuttmann, J., et al. (2019). A Coevolved EDS1-SAG101-NRG1 module mediates cell death signaling by TIR-domain immune receptors. Plant Cell *31*, 2430–2455.

Lee, A.H., Hurley, B., Felsensteiner, C., Yea, C., Ckurshumova, W., Bartetzko, V., Wang, P.W., Quach, V., Lewis, J.D., Liu, Y.C., et al. (2012). A bacterial acetyltransferase destroys plant microtubule networks and blocks secretion. PLoS Pathog. *8*, e1002523.

Li, L., Habring, A., Wang, K., and Weigel, D. (2020). Atypical resistance protein RPW8/HR triggers oligomerization of the NLR immune receptor RPP7 and autoimmunity. Cell Host Microbe *27*, 405–417.e6.

Liebschner, D., Afonine, P.V., Baker, M.L., Bunkóczi, G., Chen, V.B., Croll, T.I., Hintze, B., Hung, L.W., Jain, S., McCoy, A.J., et al. (2019). Macromolecular structure determination using X-rays, neutrons and electrons: recent developments in Phenix. Acta Crystallogr. D Struct. Biol. *75*, 861–877.

Maekawa, T., Cheng, W., Spiridon, L.N., Töller, A., Lukasik, E., Saijo, Y., Liu, P., Shen, Q.H., Micluta, M.A., Somssich, I.E., et al. (2011a). Coiled-coil domain-dependent homodimerization of intracellular barley immune receptors defines a minimal functional module for triggering cell death. Cell Host Microbe *9*, 187–199.

Maekawa, T., Kracher, B., Saur, I.M.L., Yoshikawa-Maekawa, M., Kellner, R., Pankin, A., von Korff, M., and Schulze-Lefert, P. (2019). Subfamily-specific specialization of RGH1/MLA immune receptors in wild barley. Mol. Plant Microbe Interact. *32*, 107–119.

Maekawa, T., Kufer, T.A., and Schulze-Lefert, P. (2011b). NLR functions in plant and animal immune systems: so far and yet so close. Nat. Immunol. *12*, 817–826.

Manning, G., Whyte, D.B., Martinez, R., Hunter, T., and Sudarsanam, S. (2002). The protein kinase complement of the human genome. Science *298*, 1912–1934.

Marc, J., Granger, C.L., Brincat, J., Fisher, D.D., Kao, Th, McCubbin, A.G., and Cyr, R.J. (1998). A GFP-MAP4 reporter gene for visualizing cortical microtubule rearrangements in living epidermal cells. Plant Cell *10*, 1927–1940.

Martinez-Medina, A., Flors, V., Heil, M., Mauch-Mani, B., Pieterse, C.M.J., Pozo, M.J., Ton, J., van Dam, N.M., and Conrath, U. (2016). Recognizing plant defense priming. Trends Plant Sci. *21*, 818–822.

Micali, C., Göllner, K., Humphry, M., Consonni, C., and Panstruga, R. (2008). The powdery mildew disease of Arabidopsis: a paradigm for the interaction between plants and biotrophic fungi. Arabidopsis Book *6*, e0115.

Murphy, J.M., Czabotar, P.E., Hildebrand, J.M., Lucet, I.S., Zhang, J.G., Alvarez-Diaz, S., Lewis, R., Lalaoui, N., Metcalf, D., Webb, A.I., et al. (2013). The pseudokinase MLKL mediates necroptosis via a molecular switch mechanism. Immunity *39*, 443–453.

Nakagawa, T., Suzuki, T., Murata, S., Nakamura, S., Hino, T., Maeo, K., Tabata, R., Kawai, T., Tanaka, K., Niwa, Y., et al. (2007). Improved gateway binary vectors: high-performance vectors for creation of fusion constructs in transgenic analysis of plants. Biosci. Biotechnol. Biochem. *71*, 2095–2100.

Nürnberger, T., and Brunner, F. (2002). Innate immunity in plants and animals: emerging parallels between the recognition of general elicitors and pathogen-associated molecular patterns. Curr. Opin. Plant Biol. *5*, 318–324.

Oda, Y. (2018). Emerging roles of cortical microtubule-membrane interactions. J. Plant Res. *131*, 5–14.

Pearson, J.S., and Murphy, J.M. (2017). Down the rabbit hole: is necroptosis truly an innate response to infection? Cell. Microbiol. *19*.

Petrie, E.J., Birkinshaw, R.W., Koide, A., Denbaum, E., Hildebrand, J.M., Garnish, S.E., Davies, K.A., Sandow, J.J., Samson, A.L., Gavin, X., et al. (2020). Identification of MLKL membrane translocation as a checkpoint in necroptotic cell death using monobodies. Proc. Natl. Acad. Sci. USA *117*, 8468–8475.

Petrie, E.J., Czabotar, P.E., and Murphy, J.M. (2019). The structural basis of necroptotic cell death signaling. Trends Biochem. Sci. *44*, 53–63.

Petrie, E.J., Hildebrand, J.M., and Murphy, J.M. (2017). Insane in the membrane: a structural perspective of MLKL function in necroptosis. Immunol. Cell Biol. *95*, 152–159.

Petrie, E.J., Sandow, J.J., Jacobsen, A.V., Smith, B.J., Griffin, M.D.W., Lucet, I.S., Dai, W., Young, S.N., Tanzer, M.C., Wardak, A., et al. (2018). Conformational switching of the pseudokinase domain promotes human MLKL tetramerization and cell death by necroptosis. Nat. Commun. *9*, 2422.

Plotnikova, J.M., Lynne Reuber, T., Ausubel, F.M., and Pfister, D.H. (1998). Powdery mildew pathogenesis of Arabidopsis thaliana. Mycologia *90*, 7.

Qi, T., Seong, K., Thomazella, D.P.T., Kim, J.R., Pham, J., Seo, E., Cho, M.J., Schultink, A., and Staskawicz, B.J. (2018). NRG1 functions downstream of

EDS1 to regulate TIR-NLR-mediated plant immunity in Nicotiana benthamiana. Proc. Natl. Acad. Sci. USA 115, E10979–E10987.

Quarato, G., Guy, C.S., Grace, C.R., Llambi, F., Nourse, A., Rodriguez, D.A., Wakefield, R., Frase, S., Moldoveanu, T., and Green, D.R. (2016). Sequential engagement of distinct MLKL phosphatidylinositol-binding sites executes necroptosis. Mol. Cell 61, 589–601.

Riedl, J., Crevenna, A.H., Kessenbrock, K., Yu, J.H., Neukirchen, D., Bista, M., Bradke, F., Jenne, D., Holak, T.A., Werb, Z., et al. (2008). Lifeact: a versatile marker to visualize F-actin. Nat. Methods 5, 605–607.

Rohou, A., and Grigorieff, N. (2015). CTFFIND4: fast and accurate defocus estimation from electron micrographs. J. Struct. Biol. 192, 216–221.

Rosso, M.G., Li, Y., Strizhov, N., Reiss, B., Dekker, K., and Weisshaar, B. (2003). An Arabidopsis thaliana T-DNA mutagenized population (GABI-Kat) for flanking sequence tag-based reverse genetics. Plant Mol. Biol. 53, 247–259.

RStudioTeam. (2015). RStudio (integrated development for R. RStudio, Inc.), computer software v0.90.1074. http://www.rstudio.com/.

Samson, A.L., Zhang, Y., Geoghegan, N.D., Gavin, X.J., Davies, K.A., Mlodzianoski, M.J., Whitehead, L.W., Frank, D., Garnish, S.E., Fitzgibbon, C., et al. (2020). MLKL trafficking and accumulation at the plasma membrane control the kinetics and threshold for necroptosis. Nat. Commun. 11, 3151.

Saur, I.M., Bauer, S., Kracher, B., Lu, X., Franzeskakis, L., Müller, M.C., Sabelleck, B., Kümmel, F., Panstruga, R., Maekawa, T., and Schulze-Lefert, P. (2019). Multiple pairs of allelic MLA immune receptor-powdery mildew AVRA effectors argue for a direct recognition mechanism. eLife 8, e44471.

Schindelin, J., Arganda-Carreras, I., Frise, E., Kaynig, V., Longair, M., Pietzsch, T., Preibisch, S., Rueden, C., Saalfeld, S., Schmid, B., et al. (2012). Fiji: an open-source platform for biological-image analysis. Nat. Methods 9, 676–682.

Shen, Q.H., Zhou, F., Bieri, S., Haizel, T., Shirasu, K., and Schulze-Lefert, P. (2003). Recognition specificity and RAR1/SGT1 dependence in barley Mla disease resistance genes to the powdery mildew fungus. Plant Cell 15, 732–744.

Söding, J. (2005). Protein homology detection by HMM-HMM comparison. Bioinformatics 21, 951–960.

Su, L., Quade, B., Wang, H., Sun, L., Wang, X., and Rizo, J. (2014). A plug release mechanism for membrane permeation by MLKL. Structure 22, 1489–1500.

Sun, L., Wang, H., Wang, Z., He, S., Chen, S., Liao, D., Wang, L., Yan, J., Liu, W., Lei, X., and Wang, X. (2012). Mixed lineage kinase domain-like protein mediates necrosis signaling downstream of RIP3 kinase. Cell 148, 213–227.

Tanzer, M.C., Matti, I., Hildebrand, J.M., Young, S.N., Wardak, A., Tripaydonis, A., Petrie, E.J., Mildenhall, A.L., Vaux, D.L., Vince, J.E., et al. (2016). Evolutionary divergence of the necroptosis effector MLKL. Cell Death Differ. 23, 1185–1197.

Urbach, J.M., and Ausubel, F.M. (2017). The NBS-LRR architectures of plant R-proteins and metazoan NLRs evolved in independent events. Proc. Natl. Acad. Sci. USA 114, 1063–1068.

van der Biezen, E.A., Freddie, C.T., Kahn, K., Parker, J.E., and Jones, J.D. (2002). Arabidopsis RPP4 is a member of the RPP5 multigene family of TIR-NB-LRR genes and confers downy mildew resistance through multiple signalling components. Plant J. 29, 439–451.

van Doorn, W.G. (2011). Classes of programmed cell death in plants, compared to those in animals. J. Exp. Bot. 62, 4749–4761.

Vanden Berghe, T., Linkermann, A., Jouan-Lanhouet, S., Walczak, H., and Vandenabeele, P. (2014). Regulated necrosis: the expanding network of non-apoptotic cell death pathways. Nat. Rev. Mol. Cell Biol. 15, 135–147.

Vogler, F., Konrad, S.S., and Sprunck, S. (2015). Knockin' on pollen's door: live cell imaging of early polarization events in germinating Arabidopsis pollen. Front. Plant Sci. 6, 246.

Wan, L., Essuman, K., Anderson, R.G., Sasaki, Y., Monteiro, F., Chung, E.H., Osborne Nishimura, E., DiAntonio, A., Milbrandt, J., Dangl, J.L., and Nishimura, M.T. (2019). TIR domains of plant immune receptors are NAD+-cleaving enzymes that promote cell death. Science 365, 799–803.

Wang, H., Sun, L., Su, L., Rizo, J., Liu, L., Wang, L.F., Wang, F.S., and Wang, X. (2014). Mixed lineage kinase domain-like protein causes necrotic membrane disruption upon phosphorylation by RIP3. Mol. Cell 54, 133–146.

Wang, J., Wang, J., Hu, M., Wu, S., Qi, J., Wang, G., Han, Z., Qi, Y., Gao, N., Wang, H.-W., et al. (2019). Ligand-triggered allosteric ADP release primes a plant NLR complex. Science 364.

Wang, W., Wen, Y., Berkey, R., and Xiao, S. (2009). Specific targeting of the Arabidopsis resistance protein RPW8.2 to the interfacial membrane encasing the fungal Haustorium renders broad-spectrum resistance to powdery mildew. Plant Cell 21, 2898–2913.

Weßling, R., and Panstruga, R. (2012). Rapid quantification of plant-powdery mildew interactions by qPCR and conidiospore counts. Plant Methods 8, 35.

Wu, Z., Li, M., Dong, O.X., Xia, S., Liang, W., Bao, Y., Wasteneys, G., and Li, X. (2019). Differential regulation of TNL-mediated immune signaling by redundant helper CNLs. New Phytol. 222, 938–953.

Yoo, S.D., Cho, Y.H., and Sheen, J. (2007). Arabidopsis mesophyll protoplasts: a versatile cell system for transient gene expression analysis. Nat. Protoc. 2, 1565–1572.

Zhao, J., Jitkaew, S., Cai, Z., Choksi, S., Li, Q., Luo, J., and Liu, Z.G. (2012). Mixed lineage kinase domain-like is a key receptor interacting protein 3 downstream component of TNF-induced necrosis. Proc. Natl. Acad. Sci. USA 109, 5322–5327.

Zheng, S.Q., Palovcak, E., Armache, J.P., Verba, K.A., Cheng, Y., and Agard, D.A. (2017). MotionCor2: anisotropic correction of beam-induced motion for improved cryo-electron microscopy. Nat. Methods 14, 331–332.

Zipfel, C. (2008). Pattern-recognition receptors in plant innate immunity. Curr. Opin. Immunol. 20, 10–16.

Zivanov, J., Nakane, T., Forsberg, B.O., Kimanius, D., Hagen, W.J., Lindahl, E., and Scheres, S.H. (2018). New tools for automated high-resolution cryo-EM structure determination in RELION-3. eLife 7, e42166.

STAR★METHODS

KEY RESOURCES TABLE

REAGENT or RESOURCE	SOURCE	IDENTIFIER
Antibodies		
Rat monoclonal α-HA	Sigma-Aldrich, MO, USA	Cat#11867423001; RRID: AB_390918
Mouse monoclonal α-GFP	Takara, Shiga, Japan	Cat#632375; RRID: AB_2756343
Goat α-rat IgG-HRP	Sigma-Aldrich, MO, USA	Cat#AP136P; RRID: AB_91300
Goat α-mouse IgG-HRP	Santa Cruz Biotechnology, TX, USA	Cat#Sc-516102; RRID: AB_2687626
Bacterial and Virus Strains		
Pseudomonas syringae pv. tomato (*Pst*) DC3000	Lapin et al., 2019	N/A
Pst DC3000 expressing AvrRps4	Lapin et al., 2019	N/A
Pst DC3000 expressing AvrRpt2	Bonardi et al., 2011	N/A
Pst DC3000 expressing AvrRpm1	Bonardi et al., 2011	N/A
P. fluorescens Pf0-1 *AvrRps4*	Lapin et al., 2019	N/A
Golovinomyces orontii	Lab stock	N/A
Hyaloperonospora arabidopsidis Emwa1	Lab stock	N/A
Hyaloperonospora arabidopsidis Noco2	Lab stock	N/A
Botrytis cinerea strain B05.10	Lab stock	N/A
Spodoptera frugiperda 21	Lab stock	N/A
Escherichia coli strain BL21 (DE3)	Sigma-Aldrich, MO, USA	Cat#69450
Chemicals, Peptides, and Recombinant Proteins		
Oryzaline	Sigma-Aldrich, MO, USA	Cat#36182
Latrunculin B	Abcam, Cambridge, UK	Cat#ab144291
Chitin (NA-COS-Y)	YSK, Shizuoka, Japan	N/A
Chitin ([GlcNAc]$_7$)	Elicityl, Crolles, France	Cat#GLU437
Critical Commercial Assays		
pENTR/D-TOPO	Thermo Fisher Scientific MA, USA	Cat#K240020
QuikChange Lightning site-directed mutagenesis kit	Agilent Technologies, CA, USA	210518
Ni2+-nitrilotriacetate affinity resin	Qiagen, Venla, Netherlands	Cat#30210
Superose 6	GE Healthcare, IL, USA	Cat#29-0915-96
isopropyl-β-D-thiogalactopyranoside	Sigma-Aldrich, MO, USA	Cat#10724815001
Glutathione Sepharose 4B beads	Invitrogen, CA, USA	Cat#GE17-0756-01
PreScission protease	GE Healthcare, IL, USA	Cat#GE27-0843-01
RNeasy plant mini kit	Qiagen, Venla, Netherlands	Cat#74904
Chamber slide Nunc Lab-Tek	Thermo Fisher Scientific, MA, USA	Cat#171080
Deposited Data		
Cryo-EM structure of the *At*MLKL2 tetramer		Protein Data Bank (PDB) under accession number 6LBA
Cryo-EM structure of the *At*MLKL3 tetramer		Protein Data Bank (PDB) under accession number 6KA4
raw image files, ImageJ macro file, and R scripts for image analysis		https://www.mpipz.mpg.de/R_scripts
RNA-Seq data generated in this study		Gene Expression Omnibus (GEO) database under accession number GSE129011
Experimental Models: Organisms/Strains		
A. thaliana Col-0	Lab stock	N/A
A. thaliana WT	This paper	N/A

Continued

REAGENT or RESOURCE	SOURCE	IDENTIFIER
A. thaliana mlkl1	NASC	SALK_041569c
A. thaliana mlkl2	NASC	SALK_124412c
A. thaliana mlkl3	NASC	GABI_491E02
A. thaliana mlkl12	This paper	N/A
A. thaliana mlkl13	This paper	N/A
A. thaliana mlkl23	This paper	N/A
A. thaliana mlkl123	This paper	N/A
A. thaliana eds1-2	Bartsch et al., 2006	N/A
A. thaliana MLKL1-GFP	This paper	N/A
A. thaliana MLKL1(S393D)-GFP #1	This paper	N/A
A. thaliana MLKL1(S393D)-GFP #2	This paper	N/A
A. thaliana MLKL1(S395D)-GFP	This paper	N/A
A. thaliana MLKL2-GFP	This paper	N/A
Oligonucleotides		
See Table S3		N/A
Recombinant DNA		
pGEX-6P-1-GST-*At*MLKL2	This paper	N/A
pFastBac1-*At*MLKL3-6×His	This paper	N/A
pAMPAT-35s-*At*MLKL1-HA	This paper	N/A
pAMPAT-35s-*At*MLKL1(S393D)-HA	This paper	N/A
pAMPAT-35s-*At*MLKL1(S395D)-HA	This paper	N/A
pAMPAT-35s-*At*MLKL2-HA	This paper	N/A
pAMPAT-35s-*At*MLKL2(S394D)-HA	This paper	N/A
pAMPAT-35s-*At*MLKL2(S395D)-HA	This paper	N/A
pAMPAT-35s-*At*MLKL3-HA	This paper	N/A
pAMPAT-35s-*At*MLKL3(S392D)-HA	This paper	N/A
pAMPAT-35s-*At*MLKL3(S393D)-HA	This paper	N/A
pAMPAT-35s-*At*MLKL1-mYFP	This paper	N/A
pAMPAT-35s-*At*MLKL2-mYFP	This paper	N/A
pAMPAT-35s-*At*MLKL3-mYFP	This paper	N/A
pAMPAT-35s-*At*MLKL1(1-215)-DmrB-HA	This paper	N/A
pAMPAT-35s-*At*MLKL2(1-215)-DmrB-HA	This paper	N/A
pAMPAT-35s-*At*MLKL3(1-213)-DmrB-HA	This paper	N/A
pAMPAT-35s-nLUC-DmrB-HA	This paper	N/A
pAMPAT-35s-cLUC-DmrB-HA	This paper	N/A
pGWB550-*At*MLKL1-GFP	This paper	N/A
pGWB550-*At*MLKL1(S393D)-GFP	This paper	N/A
pGWB550-*At*MLKL1(S395D)-GFP	This paper	N/A
pAMPAT-35s-*Hv*MLA$_{CC}$(1-160)-mYFP	Jacob et al., 2018	N/A
pUBQ10-mCherry-MAP4	Hamada et al., 2013	N/A
pUBQ10-mCherry-TUB6	Fujita et al., 2013	N/A
pAMPAT-35s-tagRFP-T-Lifeact	This paper (pENTR: Vogler et al., 2015)	N/A
Software and Algorithms		
MAFFT alignment software	Katoh et al., 2002	http://mafft.cbrc.jp/alignment/software/
HHSEARCH package	Söding, 2005	https://github.com/soedinglab/hh-suite
CTFFIND4	Rohou and Grigorieff, 2015	https://omictools.com/ctffind-tool
RELION	Zivanov et al., 2018	https://confluence.desy.de/display/CCS/Relion3
PHENIX	Liebschner et al., 2019	https://www.phenix-online.org/

Continued

REAGENT or RESOURCE	SOURCE	IDENTIFIER
CLC Genomics Workbench ver. 10.1.2	Qiagen, Venla, Netherlands	https://secure.clcbio.com/helpspot/index.php?pg=kb.printer.friendly&id=15
PANTHER classification system		http://pantherdb.org/
ZEN Software	Carl Zeiss	https://www.zeiss.de/mikroskopie/produkte/mikroskopsoftware/zen.html
Fiji software	Schindelin et al., 2012	https://fiji.sc/
R software	RStudioTeam, 2015	http://www.rstudio.com/

RESOURCE AVAILABILITY

Lead Contact
Further information and requests for resources and reagents should be directed to and will be fulfilled by the Lead Contact, Takaki Maekawa (maekawa@mpipz.mpg.de).

Materials Availability
All unique reagents generated in this study, including plasmid vectors used to generate transgenic plants, are available from the Lead Contact with a completed Materials Transfer Agreement.

Data and Code Availability
The atomic coordinates for the *At*MLKL2 and *At*MLKL3 structures have been deposited in the Protein Data Bank (PDB) under accession codes 6LBA and 6KA4, respectively. All sources regarding the image analysis, including the raw image files, the ImageJ macro file, and the R scripts are available at https://www.mpipz.mpg.de/R_scripts (RStudioTeam, 2015). RNA-Seq data generated in this study have been deposited in the Gene Expression Omnibus (GEO) database under accession number GSE129011.

EXPERIMENTAL MODEL AND SUBJECT DETAILS

Plant Material and Growth Conditions
The *Arabidopsis thaliana* (L.) Heynh. ecotype Columbia (Col-0) was used in this study. The T-DNA insertional mutants (Alonso et al., 2003; Kleinboelting et al., 2012) (SALK_041569c (*AtMLKL1*), SALK_124412c (*AtMLKL2*) and GABI_491E02 (*AtMLKL3*) were obtained from the Nottingham Arabidopsis Stock Centre (NASC, http://arabidopsis.info/). Double and triple mutants of *Atmlkl* were generated by crossing the T-DNA insertion lines. A segregant line derived from the cross between the *Atmlkl1* and *Atmlkl3* mutants was used as a wild-type line in addition to wild type Col-0. Each genotype was confirmed by PCR. The *eds1-2* mutant was described previously (Bartsch et al., 2006).

The transgenic lines expressing *AtMLKL1* variants or *AtMLKL2* fused to a green fluorescence protein were established in *Atmlkl1* and *Atmlkl2* mutant backgrounds, respectively. Genomic fragments including coding region and native *cis*-regulatory sequence were amplified by PCR from Col-0 genomic DNA and cloned into pENTR/D-TOPO (Thermo Fisher Scientific, Waltham, MA, USA). The phosphomimetic substitutions were introduced using the QuikChange Lightning site-directed mutagenesis kit (Agilent Technologies, Santa Clara, CA, USA). Resulting entry vectors were transferred into pGWB550 (Nakagawa et al., 2007) using LR Clonase II (Thermo Fisher Scientific). Plants were transformed by the floral dip method (Clough and Bent, 1998) with *Agrobacterium tumefaciens* strain GV3101 harbouring pMP90RK (Koncz and Schell, 1986). Plant growth conditions were described previously (Jacob et al., 2018). Primer sequences for genotyping and plasmid construction are listed in Table S3.

Bacterial Strains
Eschericha coli BL21 (DE3; Novagen) and *Agrobacterium tumefaciens* strain GV3101 harbouring pMP90RK (Koncz and Schell, 1986) were from laboratory stocks.

METHOD DETAILS

Sequence Analysis of Plant and Animal MLKLs
Sequence similarity within the animal and plant families was established by the generalized profile method (Bucher et al., 1996). Sequences were aligned by the L-INS-I method of the MAFFT alignment software (Katoh et al., 2002), followed by minor manual editing of ambiguously aligned regions. Sequence similarity between the animal and plant MLKL families was established by Hidden Markov Model (HMM)-to-HMM comparison using the HHSEARCH package (Söding, 2005). The 99,696 orthogroups (OGs) among 52 plant species have been established recently (Lapin et al., 2019). An OG containing *At*MLKLs was used for the Neighbor-Net analysis of

codon-aligned nucleotide sequence as descried previously (Maekawa et al., 2019). The sequence from the papaya genome was excluded in this study.

Protein Expression and Purification

Full length *At*MLKL3 (residues 1-701) with an engineered C-terminal 6×His tag was generated by standard PCR-based cloning strategy and its identity was confirmed by sequencing. The protein was expressed in Sf21 insect cells using the vector pFastBac 1 (Invitrogen). One litre of cells (2.5×10^6 cells ml^{-1}, medium from Expression Systems) was infected with 20 ml baculovirus at 28°C. After growth at 28°C for 48 hours, the cells were harvested, re-suspended in a buffer containing 50 mM Tris-HCl pH 8.0 and 300 mM NaCl, and lysed by sonication. The soluble fraction was purified from the cell lysate using Ni^{2+}-nitrilotriacetate affinity resin (Ni-NTA, Qiagen). The protein was then further purified by further purified by gel filtration (Superose 6, 10/30; GE Healthcare). For cryo-EM investigations, the purified protein was concentrated to 0.3 mg/mL in buffer containing 50 mM Tris-HCl pH 8.0, 300 mM NaCl and 3 mM DTT.

The construct of full length *At*MLKL2 (residues 1-711) with N-terminal GST tag was cloned into the pGEX-6P-1 vector (GE Healthcare), and was expressed in *Escherichia coli* strain BL21(DE3; Novagen) at 16 °C. After isopropyl-β-D-thiogalactopyranoside (IPTG; Sigma) induction for 12 h, cells were harvested and re-suspended in buffer containing 50 mM Tris-HCl pH 8.0 and 300 mM NaCl, and lysed by sonication. The soluble fraction was purified from the cell lysate using Glutathione Sepharose 4B beads (Invitrogen). The proteins were then digested with PreScission protease (GE Healthcare) to remove the GST tag and further purified by gel filtration (Superose 6, 10/30; GE Healthcare). For cryo-EM investigations, the purified protein was concentrated to 0.3 mg/mL in buffer containing 50 mM Tris-HCl pH 8.0, 300 mM NaCl and 3 mM DTT.

Cryo-EM Analysis

For cryo-EM analysis, an aliquot of 3.5 μl *At*MLKL2 or *At*MLKL3 protein was applied to a holey carbon grids (Quantifoil Cu 1.2/1.3, 200 mesh) glow-discharged (Harrick Plasma) with a middle force for 30 s after evaluating for 2 min. The grids were blotted by a pair of 55 mm filter papers (TED PELLA, INC.) for 3-3.5 s at 8 °C with 100% humidity and flash-frozen in liquid ethane using a FEI Vitrobot Marked IV. Cryo-EM data were collected on Titan Krios electron microscope operated at 300 kV and a Gatan K2 Summit direct electron detection camera (Gatan) using eTas. Micrographs were recorded in super-resolution mode at a nominal magnification of 22500 ×, resulting in a physical pixel size of 1.30654 Å per pixel. Defocus values varied from -1.7 μm to -2.3 μm for data set. The dose rate was 10.6 electron per pixel per second. Exposures of 8.0 s were dose-fractionated into 32 sub-frames, leading to a total accumulated dose of 50 electrons per Å^2. In total, two batches of data were collected, one for *At*MLKL3 and another for *At*MLKL2.

Image Processing and 3D Reconstruction

A total of 1,434 and 1,828 raw images stacks of *At*MLKL3 and *At*MLKL2 acquired under super-resolution mode, were 2x binned processed using MotionCor2 (Zheng et al., 2017), generating aligned, dose-weighted and summed micrographs in a pixel size of 1.30654 Å per square pixel. CTFFIND4 (Rohou and Grigorieff, 2015) was used to estimate the contrast transfer function (CTF) parameters. After the removal of bad micrographs via the evaluation of CTF parameters, remaining images were processed in RELION (Zivanov et al., 2018). Approximately 2,000 particles were manually picked and 2D-classified to generate templates for auto-picking. 983,779 and 1,135,463 autopicked particles for *At*MLKL3 and *At*MLKL2 respectively were then used for reference-free 2D classification, to remove contaminants and bad particles. The remaining good particles were subjected to 3D classification using initial 3D reference model obtained by *ab initio* calculation from Relion3.0. Particles from good classes that possess density map with better overall structure features were selected for the 3D refinement. The final 3D refinement using D2 symmetry resulted in reconstructions of *At*MLKL3 and *At*MLKL2 tetramer at resolution of 3.4 Å and 4.1 Å, the resolutions were determined by gold-standard Fourier shell correlation. Local resolution distribution was evaluated using Relion.

Model Building and Refinement

Electrostatic potential density of *At*MLKL3 was used to build the model de novo, as the overall resolution of map density was sufficient to display side chains. The model of *At*MLKL3 was manually built into the density in COOT(Brown et al., 2015), and was refined against the EM map by PHENIX(Adams et al., 2010) in real space with secondary structure and geometry restraints. The refined *At*MLKL3 model was docked into the density of *At*MLKL2. The sequence of the docked *At*MLKL3 model was changed to that of *At*MLKL2 under COOT and the *At*MLKL2 model with corrected sequence was subjected to refinement by PHENIX. The C-terminal serine-rich region of *At*MLKL2 or *At*MLKL3 is much less well defined in the density and is not included in the models. Final model of *At*MLKL3 and *At*MLKL2 was validated using MolProbity and EMRinger in PHENIX package. The structures of human MLKL (Su et al., 2014) and mouse MLKL (Murphy et al., 2013) were used for the superposition of the HeLo domains as shown in Figure 3A. Table S2 summarizes the model statistics.

RNA Sequencing

Total mRNA from leaves was obtained at 48 hours after challenge with conidia of *Golovinomyces orontii* using the RNeasy plant mini kit (Qiagen). At this time point *G. orontii* develops initial hyphae following establishment of the first haustorium inside a host cell (Micali et al., 2008). RNA sequencing (RNA-Seq) libraries were prepared by the Max Planck Genome Centre Cologne (Cologne, Germany) using the Illumina TruSeq stranded RNA sample preparation kit (Illumina). The resulting libraries were subjected to 150-bp single-end

sequencing using the Illumina HiSeq3000 (Illumina). Mapping of sequenced reads onto the *Arabidopsis thaliana* gene model (TAIR10), principal component analysis, and differential gene expression analysis were performed in the CLC Genomics Workbench (Qiagen, ver. 10.1.2) using the tool 'RNA-Seq with the default parameter setting. The data derived from Col-0 and WT were pooled as data of wild-type lines in the analysis. The heat map of 93 genes differentially expressed between wild type lines and *Atmlkl* mutants (|log$_2$FC| >1 and false discovery rate (FDR) < 0.05) were generated using the R package (ver. 1.08) with the pheatmap function. Gene ontology enrichment analysis was performed using the PANTHER classification system (http://pantherdb.org/) with default settings for *Arabidopsis thaliana*.

Transient Gene Expression in Protoplasts

Isolation, transfection and luciferase activity measurement of Arabidopsis protoplasts were performed as described previously (Saur et al., 2019). Protoplasts were isolated from the leaves of two-week-old *Arabidopsis* plants grown in liquid 1 x Murashige and Skoog medium. Coding sequences (CDS) of *AtMLKL1* and *AtMLKL2* without stop codons were initially cloned into pENTR/D-TOPO (Thermo Fisher Scientific). The CDS of *AtMLKL3* without a stop codon was chemically synthesized and cloned into pENTR221 (Thermo Fisher Scientific). Two synonymous substitutions (G1371T and A1413G) were introduced into *AtMLKL3* CDS to remove restriction sites that hamper the DNA synthesis. Entry clones were transferred into the Gateway cloning-compatible pAMPAT-GW-mYFP, pAMPAT-GW-3xHA, or pAMPAT-GW expression vectors (Maekawa et al., 2011a), which are derivatives of pAMPAT-MCS (accession number: AY436765). Primers sequences of for plasmid construction are listed in Table S3. pENTR-tagRFP-T-Lifeact (Vogler et al., 2015) was transferred into pAMPAT-GW. The expression vectors for *Hv*MLA(1–160aa), MAP4 and Tub6 were described previously (Fujita et al., 2013; Hamada et al., 2013; Maekawa et al., 2011a).

Protoplast Viability Assay

Following protoplast transfection and regeneration, Evans blue dye dissolved in water was added to the samples to a final concentration of 0.04% (w/v). The stained cells were examined under a standard microscope. For luciferase-based viability assay luciferase and *At*MLKL expression constructs were co-transfected into protoplasts (approx. 1.5 x 10^5 cells/transfection) and luciferase activity was measured as a proxy of cell viability.

Induced Oligomerization

Two domains of FKBP (F36V) tagged with HA without N-myristoylation signal were PCR amplified from pC4M-FV2E plasmid (ARIAD, Cambridge, MA, USA). *Nco*I and *Hind*III restriction sites were added to the 5' end of forward and reverse primers, respectively. The digested PCR fragment with *Nco*I and *Hind*III were ligated into the same restriction sites present between the attR2 and the terminator sequences of pAMPAT-GW expression vector. The resulting vector is named pAMPAT-GW-FV2E-HA. Coding regions corresponding to the N- and C-terminal luciferase fragments (nLUC and cLUC) were PCR amplified from nLUC and cLUC expression vectors (Gehl et al., 2011) and cloned into pENTR/D-TOPO. Respective entry clones were transferred into pAMPAT-GW-FV2E-HA. B/B homodimerizer (also known as AP20187 ligand) was purchased from Takara Bio, Japan. After transfection, protoplasts in incubation buffer (i.e. WI solution (Yoo et al., 2007)) were separated into two tubes and added the same amount of incubation buffer supplemented with B/B homodimerizer (250 nM at the final concentration) or ethanol as solvent control. Primer sequences for the plasmid construction are listed in Table S2. We were able to reconstitute luciferase activity of co-expressed N- and C-terminal halves of luciferase fused to 2x DmrB domains in a ligand-specific manner (Figure S5G) and the ligand itself did not affect the luciferase reporter assay in protoplasts (Figure S5H).

Pathogen Infection Assays

The *G. orontii* infection assay was performed as described previously (Weßling and Panstruga, 2012). *G. orontii* DNA was quantified by qPCR at indicated time points after inoculation of conidia and normalised using the amount of plant specific gene (AT3G21215). The *Hpa* infection assay was performed as previously described (Cabral et al., 2011). Lactophenol-trypan blue staining was described previously (Bai et al., 2012). The *B. cinerea* strain B05.10 was used in this study. Droplet inoculation of six-week-old plants was performed as described previously (Birkenbihl et al., 2012), except that 2 μl of the spore solution were used on each side of the leaf and two leaves of similar age were used per plant. *B. cinerea* DNA was quantified by qPCR as previously described (Gachon and Saindrenan, 2004). *Pseudomonas syringae* pv. *tomato* (*Pst*) DC3000 and *Pst* DC3000 expressing *AvrRps4*, *AvrRpt2* or *AvrRpm1* and *Pseudomonas fluorescens* Pf0-1 expressing *AvrRps4* (Lapin et al., 2019) were used in this study. *Pst* growth assays and ion leakage measurement following bacterial infiltration were performed as described previously (Jacob et al., 2018). In the *Hpa* infection assay, data were obtained in three independent experiments, including two and one biological replicates for Emwa1 (n=6) and Noco2 (n=3), respectively. In the *Pst* DC3000 infection assay, data were obtained in five independent experiments, each including six biological replicates for *AvrRps4* (n=36), two independent experiments, each including three biological replicates for *AvrRpm1* (n=6), four independent experiments, each including one biological replicate for *AvrRpt2* (n=4), and three independent experiments, each including one biological replicate without avirulence effectors (n=3). In the *B. cinerea* infection assay, data were obtained in three independent experiments (n=3). In the ion leakage measurement, data were obtained in three independent experiments, each including six biological replicates for the *AvrRPS4* (n=18) and one biological replicate for the *AvrRpm1* (n=3).

Immunoblot Assays

Primary antibodies were monoclonal antibodies from mouse: α-GFP (JL-8, 1:5000, Takara, Shiga, Japan) or rat: α-HA (3F10, 1:1000, Sigma-Aldrich, St. Louis, MO, USA). Goat α-mouse IgG-HRP (1:10000, Santa Cruz Biotechnology, Dallas, TX, USA) or goat α-rat IgG-HRP (1:10000, Sigma-Aldrich) were used as secondary antibodies. The detailed procedure is described in (Jacob et al., 2018).

Biolistic Transient Gene Expression

Biolistic delivery of plasmid DNA into the abaxial epidermis of leaves was essentially performed as described previously (Shen et al., 2003). Leaves were detached immediately before bombardment and the bombarded leaves were transferred to 1% agar plates supplemented with 85 μM benzimidazole and incubated at 20°C for 15 h before confocal microscopy.

Confocal Microscopy

Transfected protoplasts in a chamber slide (Nunc Lab-Tek, Thermo Fisher Scientific) with incubation buffer (i.e. WI solution, (Yoo et al., 2007)) or 2-5 mm leaf discs prepared form rosette leave of 4-5-week-old plants were observed under a confocal microscope (LSM880, Carl Zeiss, Germany) equipped with a 40X water-immersion and a 63X oil-immersion objective. Lambda stack images were obtained for spectral imaging. Images were analyzed and processed with ZEN Software (Carl Zeiss) and ImageJ (NIH). In Figure 7B, confocal images were acquired over time (for wild type, 124 seconds; for S393D, 194 seconds; for S395D, 166 seconds) and used for maximum intensity projection (bottom panels). Representative single frame images are shown (top panels).

Chitin Treatment and Image Analysis

Three to four-day-old dark-grown *Arabidopsis* plants expressing *At*MLKL1-GFP grown on 1 x Murashige and Skoog solid medium were gently transferred to water (mock), 1 mg/ml NA-COSY (YSK, Shizuoka, Japan) in water or 10 μM [GlcNAc]$_7$ (ELICITYL, Crolles France) in water. After 3∼4 hours of chitin treatment, GFP signals from the epidermis of hypocotyls were examined using a confocal microscope (LSM880, Carl Zeiss) with a 63X oil-immersion objective. Airyscan processing was done by ZEN2012 (Carl Zeiss). Processed images were analyzed with Fiji software (Schindelin et al., 2012), as follows: The pixel size of each image was adjusted to that of the smallest (0.019 μm/pixel) and the background was subtracted with the rolling ball radius of 5 pixels. The first frame image was used to detect particles after the *autothreshold* function with the MaxEntropy method and the *watershed* function. These regions of interest (ROIs) were used to measure the average intensity across the image stack. In total, 2,390 particles from 19 images were analyzed. The following data analysis was performed with R software (https://www.r-project.org/). For each ROI, 20% of the initial intensity was set as the local threshold, and three consecutive frames above and below the local threshold were recognized as "visit" and "leave", respectively, to deal with stochastic fluctuations of the signal. The visit-leave pattern was used to calculate the Run Length Encoding with the *rle* function of the base package and the total number of frames and the total number of frames that had the particle visiting was defined as the "total time of visit". When the first visit was no longer than two frames, the particle was defined as a "mobile particle".

QUANTIFICATION AND STATISTICAL ANALYSIS

Statistical significances correspond to Tukey's HSD test or Student's T-test as indicated in the respective figure legends.